Particle and Fibre Toxicology

RESEARCH

Open Access

Brain iron accumulation in neurodegenerative disorders: Does air pollution play a role?

Jithin V. George[1], Kathryn J. Hornburg[4], Alyssa Merrill[1], Elena Marvin[1], Katherine Conrad[1], Kevin Welle[2], Robert Gelein[1], David Chalupa[1], Uschi Graham[3], Günter Oberdörster[1], G. Allan Johnson[4], Deborah A. Cory-Slechta[1*] and Marissa Sobolewski[1*]

Abstract

Background Both excess brain Fe and air pollution (AP) exposures are associated with increased risk for multiple neurodegenerative disorders. Fe is a redox-active metal that is abundant in AP and even further elevated in U.S. subway systems. Exposures to AP and associated contaminants, such as Fe, are lifelong and could therefore contribute to elevated brain Fe observed in neurodegenerative diseases, particularly via nasal olfactory uptake of ultrafine particle AP. These studies tested the hypotheses that exogenously generated Fe oxide nanoparticles could reach the brain following inhalational exposures and produce neurotoxic effects consistent with neurodegenerative diseases and disorders in adult C57/Bl6J mice exposed by inhalation to Fe nanoparticles at a concentration similar to those found in underground subway systems (~ 150 μg/m^3) for 20 days. Olfactory bulb sections and exposure chamber TEM grids were analyzed for Fe speciation. Measures included brain volumetric and diffusivity changes; levels of striatal and cerebellar neurotransmitters and trans-sulfuration markers; quantification of frontal cortical and hippocampal Aβ42, total tau, and phosphorylated tau; and behavioral alterations in locomotor activity and memory.

Results Particle speciation confirmed similarity of Fe oxides (mostly magnetite) found on chamber TEM grids and in olfactory bulb. Alzheimer's disease (AD) like characteristics were seen in Fe-exposed females including increased olfactory bulb diffusivity, impaired memory, and increased accumulation of total and phosphorylated tau, with total hippocampal tau levels significantly correlated with increased errors in the radial arm maze. Fe-exposed males showed increased volume of the substantia nigra pars compacta, a region critical to the motor impairments seen in Parkinson's disease (PD), in conjunction with reduced volume of the trigeminal nerve and optic tract and chiasm.

Conclusions Inhaled Fe oxide nanoparticles appeared to lead to olfactory bulb uptake. Further, these exposures reproduced characteristic features of neurodegenerative diseases in a sex-dependent manner, with females evidencing features similar to those seen in AD and effects in regions in males associated with PD. As such, prolonged inhaled Fe exposure via AP should be considered as a source of elevated brain Fe with aging, and as a risk factor for neurodegenerative diseases. The bases for dichotomous sex effects of inhaled Fe nanoparticles is as of yet unclear. Also as of yet unknown is how duration of such Fe exposures affect outcome, and/or whether exposures to inhaled Fe

*Correspondence:
Deborah A. Cory-Slechta
deborah_cory-slechta@urmc.rochester.edu
Marissa Sobolewski
marissa_terry@urmc.rochester.edu
Full list of author information is available at the end of the article

during early brain development enhances vulnerability to subsequent Fe exposures. Collectively, these findings suggest that regulation of air Fe levels, particularly in enclosed areas like subway stations, may have broad public health protective effects.

Keywords Iron, Air pollution, Tau, Olfactory bulb, Memory, Alzheimer's disease, Parkinson's disease, Substantia nigra

Background

Excess brain iron (Fe) accumulation above that seen with normal aging is characteristic of numerous neurodegenerative diseases and disorders [1, 2], and, given the redox activity of Fe, therefore often considered to play a key role in the etiology of these disorders [3]. Brain Fe levels are elevated in Alzheimer's disease (AD), a female-biased disorder characterized by cognitive decline and brain accumulation of beta amyloids and tau, without concurrent elevations in serum Fe [4, 5]. Cortical Fe levels have been found to correlate with the Braak staging of the severity of AD [6]. Fe accumulation is also seen in substantia nigra and the red nucleus [7] in early stages of Parkinson's Disease (PD), a male-biased neurodegenerative disease resulting from the loss of dopamine neurons in substantia nigra that lead to motor impairments [8]. Further, elevated brain Fe has been shown to be negatively associated with general cognitive ability [9], and cognitive impairments in both AD and PD [10–12].

Despite the historical recognition of elevated brain Fe content in neurodegenerative diseases and disorders, the basis for this accumulation is not known, but has been ascribed to e.g., dysregulation of Fe homeostasis [13] or breakdown of the blood brain barrier [14]. What has never been considered, however, is the hypothesis that exposure to Fe via air pollution (AP) may play a primary role in elevating exogenous Fe levels in brain, and promoting dysregulation of endogenous Fe homeostasis via uptake of exogeneous Fe-laden nanoparticles. Indeed, Fe constitutes one of the most abundant metal contaminants of AP [15], and exposures to AP are life-long. AP is a dynamic and complex mixture of gases (e.g., SO_2 and NO_x) and particulate matter (PM), with PM defined by particle size (i.e., coarse particles or PM_{10}= ≤10 um, fine particles or $PM_{2.5}$= ≤2.5 um; ultrafine particles or UFP or $PM_{0.1}$= ≤100 nm) [16]. The UFP component is considered the most reactive component of AP due to its greater surface area/mass ratio for adherence of contaminant particles that include Fe and other trace elements [17], coupled with its ability to travel directly from the nose into the brain via olfactory axons, bypassing the blood brain barrier [18, 19], which could explain the corresponding lack of any consistent elevations in serum Fe in AD and PD [20, 21].

Correspondingly, AP exposures have been associated with multiple neurodegenerative diseases, including both AD and PD [22–26]. Exposures to $PM_{2.5}$ (size fractions ≤2.5 um) AP have been associated with reduced memory and processing speed [27] and increased cognitive impairment [28], with some studies suggesting a more pronounced impact in women [29]. Both PD and AD diagnoses has been correlated with levels of NO_x [30]. AP exposures alter brain structure, with reports of reductions in both white matter and gray matter volumes [31, 32]) and in hippocampal volume [33] and size of the corpus callosum, and with ventriculomegaly and brain infarcts [34–38]. Collectively, these findings are supported by studies in animal models of both AD and of PD [28, 39, 40].

Fe is one of the most abundant metals in AP [15]. Fe levels in air measured at 13 sites in the U.S. averaged 108 ng/m^3 with a range of 41–240 ng/m^3 [41, 42], but broad spatial variation occurs based on emission sources [15]. For example, ambient PM exposures in underground U.S. subway systems were recently estimated to range from 112 ± 46.7 to 779 ± 249 μg/m^3 [43, 44] and in other studies from 141 ± 81.1 to 329 ± 116 μg/m^3 [45]. While Fe in ambient AP from different sources can occur in water-soluble ($Fe2^+$) forms [46], it can also be present as Fe (II, III) oxides: i.e., magnetite (Fe_3O_4) and hematite (Fe_2O_3) [47–50]. Analysis of Fe speciation is critical, as solubility and bioavailability of these metals influence redox potential that can produce oxidative stress. Magnetite nanoparticles, a mixed oxide with Fe^{2+}/Fe^{3+}, have been found in human postmortem brain samples [48, 51], and brain magnetite has been linked to the incidence of AD [52, 53] and directly associated with both Aβ plaques and tau tangles [54, 55].

Taken together, these data highlight the need to evaluate the neurotoxicity of inhaled Fe-oxide nanoparticles in AP and their potential relationship to neurodegenerative disorders such as AD and PD. For that purpose, the current study sought to confirm in a mouse model that: (i) brain uptake of exogenous Fe nanoparticles via inhalation exposure occurs, and (ii) to examine the hypothesis that inhalation of such Fe oxide nanoparticles could reproduce features of neurodegenerative diseases/disorders in a mouse model. The focus of the consequences of the exposures included some features unique to AD and PD, as well as some features shared across neurodegenerative diseases and disorders [56].

Methods

Animals and husbandry

Male and female young adult (10 weeks old) C57Bl/6 J mice (Jackson Laboratories) were placed in same-sex pairs and housed in standard mouse caging and maintained at 22 + − 2 °C on a 12-h light–dark cycle (lights on at 06:00) at the University of Rochester Medical Center. Cages were provided with approximately 3 mm high performance bedding (BioFresh), ad libitum standard rodent chow (LabDiet Autoclavable Diet 5010), and water. Male and female mice were randomly assigned to either control or Fe-exposure groups. A subset of mice were euthanized at 48 h post final Fe exposure (Fig. 1) and brains were collected for Fe speciation analyses, magnetic resonance histological (MRH) analyses (n = 3/4 sex/treatment group), and analyses of neurotransmitter levels (n = 6/sex/treatment group) in frontal cortex and cerebellum. An additional subset of mice were randomly selected for behavioral assessments after which brains were collected (n = 12/sex/treatment group) following euthanization at approximately 6 mos post-exposure, for evidence of protein aggregation and brain neurotransmitter levels. Body weights were obtained every other day to monitor for potential systemic toxicity and experiments carried out in accordance with protocols approved by the Institutional Animal Care and Use Committees at the University of Rochester. For all mouse behavioral experiments and biochemical assessments, mouse/samples were counterbalanced by treatment group and sex to ensure any temporal or experimental variation was distributed across all groups.

Fe oxide: electric spark generation and exposure

Mice were exposed via inhalation to Fe oxide in compartmentalized whole body exposure chambers using an intended Fe concentration of 100 μg/m^3, chosen to be below the range of values cited for Fe levels in subways. Exposures were carried out for 2 h per day [45]. Mice were exposed for 5 days/week (M-F) over one month (July 8th, 2021 to August 6th, 2021) for a total of 20 exposure sessions. This exposure paradigm was roughly designed based on Organisation for Economic Co-Operation and Development (OECD) subacute inhalation toxicity study guidelines [57]. Whole-body inhalation exposures were conducted in the University of Rochester Inhalation Core Facility in single-house 30L stainless-steel reinforced Lexan exposure chambers. Control mice were exposed to HEPA-filtered air; experimental mice were exposed to Fe-oxide UFP particles generated by electric spark discharge in argon between two 99.99% pure iron rods (3N5 Purity, ESPI Metals, Ashland, OR, USA) using a GFG-1000 Palas generator (Palas GmbH, Karlshrue, Germany) in an argon atmosphere. Airborne particles were passed through a deionizer so that particles reached Boltzmann equilibrium charge. Particle number concentration was controlled by spark discharge frequency. Aerosol number concentration and particle size were monitored in real-time via a Condensation Particle Counter (CPC, model 3022, TSI Inc, St Paul, MN, USA) and Scanning Mobility Analyzer (SMPS, model 3934 TSI Inc, St Paul, MN, USA) respectively.

The Fe-oxide particles (FeO, Fe_2O_3, and Fe_3O_4 nanoparticles) were generated by adding a low flow of oxygen (~ 50 mL/min) into the argon flow (~ 5 L/min) which then entered the spark discharge chamber. An O_2 sensor (MAXO2-250E, Maxtec, Salt Lake City, UT, USA) confirmed the maintenance of an oxygen concentration of 21% in the exposure chamber. Resultant particle sizes

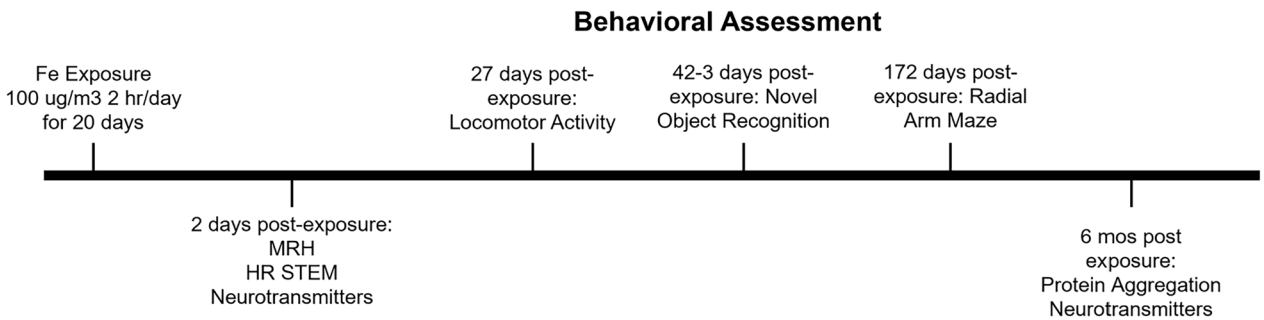

Fig. 1 Schematic of experimental design. 32 young adult male and 32 young adult female mice were exposed via inhalation to 100 μg/m^3 Fe oxide nanoparticles or filtered air for 2 h/day for 5 days/week (M–F) for a total of 20 exposure sessions. Brains were collected from a subset of each sex/treatment group at 2 days post exposure for Fe speciation analyses, magnetic resonance histological analyses and quantification of brain neurotransmitter levels. Six mice from each sex/treatment group were subjected to behavioral testing over approximately 6 months after which brains were collected for determination of neurotransmitter levels and quantification of Aβ42 and Tau

were exclusively in the ultrafine size range with a count median diameter (CMD) of approximately 30–34 nm. Mass concentrations were determined gravimetrically by filter weight (25 mm, Emfab Membrane Filters, Pall Life Sciences, Port Washington, NY) collected twice daily (5 L/min for 60 min., 300L total volume) from the filtered air and ultrafine Fe-oxide particle exposure chambers and secondarily determined using ICP-MS data. Electrostatic precipitation was used to collect particles on transmission electron microscopy (TEM) grids made of copper.

Magnetic resonance histology

Magnetic resonance histology (MRH) was performed using methods previously described [58], conducted similarly to magnetic resonance imaging, except in post-mortem tissue. Briefly, mice were perfusion-fixed using an active stain of buffered formalin and Prohance, a Gd contrast agent used to reduce the spin lattice relaxation time (T1) with imaging using a 9.4 T vertical bore magnet [58]. These specimens use the same diffusion weighted imaging protocol that has been ported to a 7 T horizontal bore magnet with similar, gradient, and rf coils. A 3D spin echo Steskal Tanner sequence was used with TR/TE = 100/15.8 ms with isotropic spatial resolution of 35 microns. Forty-six 3D volumes were acquired with b values of 3000 s/mm^2 with b vectors that uniformly sample the unit sphere. Five baseline (b0) volumes were acquired. All data was acquired with compressed sampling using an acceleration of 8X and reconstructed using the iterative methods described in [59]. Labels were applied using the methods described in [58]. The labels (r1CCFv3) are consistent with the Allen Brain Atlas common coordinate framework with modifications to accommodate quantitative connectomics. The b0 volumes were registered together. The 46 diffusion weighted volumes were registered to this average baseline to reduce the consequences of eddy current. The resulting 4 dimensional volume was post processed in DSI Studio (https://dsi-studio.labsolver.org/) yielding the following quantitative scalar images: axial diffusivity (AD), mean diffusivity (MD), radial diffusivity (RD), fractional anisotropy (FA), color fractional anisotropy (clrFA) all of which provide insight into the tissue cytoarchitecture [60].

Behavioral assessment

Locomotor activity

Spontaneous locomotor activity was measured in one 60-min session in chambers (27.3 cm × 27.3 cm × 20.3 cm) with 48-channel infrared photobeams (Med Associates Inc., St. Albans, Vermont). Photobeam breaks were recorded across five-minute intervals for 60 min using measures of stereotypic, vertical, and ambulatory movements as well as ambulatory distance and time in center vs. edge zones. Stereotypic counts were defined as localized movement, i.e., the number of beam breaks within a 2 × 2 inch photobeam box when non-ambulatory. Vertical counts were defined as the total time that z-axis photobeams or photobeams that were 7 cm above the floor of the locomotor box were broken. Ambulatory counts were defined as the number of photobeam breaks during ambulatory movement, and ambulatory distance was defined as the differences in angular movements. Time in zone was defined as the total time spent within a given zone. Resting time was defined as time spent with no new photobeam breaks. Zone entries were defined as entry of all four paws into a given zone. The locomotor arena was broken into two zones: the center zone (center 15.7 × 15.7 cm square) or edge zone (space between center square and arena boundaries).

Novel object recognition memory (NOR)

Measurement of locomotor activity was followed by NOR assessment which consisted of two sessions conducted in an open plexiglass arena (30.5 cm × 30.5 cm × 30.5 cm). In the first session, mice were placed individually into the test chamber containing two small round white knobs secured to the chamber floor, and were allowed to explore the chamber and objects for 10 min familiarize them with the sample objects and for assessment of potential side preference. A second session occurred 24 h later to assess memory of the previously observed sample objects. In session 2, mice were returned to the testing chamber, which now retained one small round white knob (sample object) but also included a small square, black knob (novel object) in place of the prior white knob. Position of the novel object (right or left side) was counterbalanced across treatments and subjects to preclude side bias. Sessions were videotaped and scored using Noldus software (The Observer XT, Noldus) by a trained observer blinded to treatment condition. Object exploration was defined as a mouse being oriented toward the object with its head crossing a pre-marked 2 cm circle surrounding the object. Object recognition was analyzed using three different indices which control for differences in overall exploration across mice: duration index (total novel exploration time/[total novel time + total sample time]), bout index (total novel bouts / [total novel bouts + total sample bouts]), and time-per-bout index (average novel time per bout / [average novel time per bout + average sample time per bout]).

Radial arm maze (RAM)

Following NOR testing, RAM performance was evaluated in radial arm maze consisting of 8 arms emanating from a center arena. Mice were first food restricted until they reached 85% of free-feeding body weight, and

then habituated to the radial arm maze in two sessions separated by 24 h. In the first habituation session, two mice from the same cage were placed in the maze and allowed to freely explore. For the second habituation session, mealworms were placed at the end of each arm of the maze and mice were individually introduced to the maze to freely explore for five minutes.

In subsequent experimental sessions beginning 48 h after the second habituation session, mealworms were placed in odd- or even-numbered arms, with placement counterbalanced by sex and treatment group. Mice were placed in the center of the maze for five seconds with all arm doors closed, after which doors were simultaneously opened and mice allowed to freely explore the maze. Arm entry was defined as all four paws within an arm, past the arm door. If a mouse entered an arm, the door to the arm closed until the reward was completely consumed or for a total of five seconds. This process was repeated until all rewards were consumed or until the ten-minute maximum session time ended, whichever occurred first. The maze was thoroughly cleaned with disinfectant between each test session. Male mice underwent 5 test sessions, while female mice underwent 3 test sessions due to disruptions by construction-related activity. Number of correct entries, number of incorrect entries or working memory errors (defined as repeat entries to arms after reward was already consumed), and time to obtain all rewards were recorded. Percent error was calculated as the ratio of number of incorrect entries to total number of entries multiplied by 100.

Aβ42, total and pS199 Tau protein quantification

At approximately postnatal day 270, hippocampus, frontal cortex, and striatum were dissected from brain, and amyloid beta 42, total tau, and pS199 tau concentrations measured in duplicate using commercially available immunoassay kits (Invitrogen, Waltham, MA, USA, catalogue KMB3441, KMB7011 and KMB7041 respectively) according to the manufacturer's specifications. Samples were read on a SynergyH1 Hybrid Reader (BioTek, Winooski, VT, USA) with Gn5 2.01 software. Sample replicates with coefficient of variation (COV) higher than 15% were excluded from the analysis. Standard curve CVs fell below 10%.

Brain neurotransmitter levels

Striatal and cerebellar concentrations of dopamine (DA), 3–4-dihydroxyphenylacetic acid (DOPAC), homovanillic acid (HVA), tyrosine (Tyr), norepinephrine (NE), glutamine (Gln), glutamate (Glu), gamma-aminobutyric acid (GABA), tryptophan (Trp), kynurenine (Kyn), serotonin (5HT) and 5-hydroxyindoleacetic acid (5HIAA) were measured in brains collected 48 h post-exposure to Fe and in another subset of mice at approximately PND270. For this purpose, hemisected brain tissue was thawed and diluted with approximately 75 µL of ice-cold acetonitrile (50%, v/v) normalized to weight and homogenized via sonication for 10 s (SLPe digital sonifier, Branson Ultrasonics Corp., Danbury, CT.). Samples sat for ten minutes after which homogenates were collected and centrifuged at 10,000 *g* for 20 min and 4 °C. The new supernatant was then collected and stored at − 80 °C until LC–MS analysis.

Stock solutions of the above analytes were made at 5 mg/mL in ddH_2O, except Tyr which was made in 0.2 M HCl. To study endogenous neurotransmitter variations within specific regions, standard solutions were made with ddH2O with analyte concentrations ranging as per prior range-finding studies. The solution was then derivatized using 13C6 benzoyl chloride (BzCl, Sigma Aldrich) as previously described [61] to create individual neurotransmitter internal standards. Internal standards were aliquoted and stored at − 80 °C until LC–MS analysis. Prior to analysis, internal standard mixtures were thawed, diluted in 50% acetonitrile and mixed with 1% sulfuric acid. This mixture was then added to derivatized samples. Samples were then centrifuged at 16,000 *g* for five minutes and 20 µL of supernatant collected into a LoBind tube (Eppendorf). 10 µL of 100 mM sodium carbonate, 10 µL of 2% BzCl in acetonitrile, and 10 µL of internal standard were added sequentially to the LoBind tube. 50 µL of ddH2O was then added to reduce organic concentration and then, samples were centrifuged to remove any remaining protein pellets. The resulting supernatant was added to an autosampler vial.

LC–MS/MS analysis was carried out by a Dionex Ultimate 3000 UHPLC coupled to a Q Exactive Plus mass spectrometer (Thermo Fisher). Analytes were separated on a Waters Acquity HSS T3 column. The mobile phases were: 10 mM ammonium formate in 0.1% formic acid, and also, acetonitrile. The flow rate was set to 400 µL/min and the column oven was set at 27 °C. After 5 µL of each sample was injected, the analytes were separated using a 12-min multi-step gradient. The Q Exactive Plus was operated in positive mode, and a parallel reaction monitoring method (PRM) was used to detect derivatized molecules. Fragment ions were extracted with a 10 ppm mass error using the LC Quan node of the Xcalibur software (Thermo Fisher). Endogenous analyte peak areas were compared to those of each internal standard to determine relative abundance. Turnover of neurotransmitters was also calculated including Gln/Glu, Glu/GABA, 5HIAA/5HT, HVA/DA and DOPAC/DA.

Fe nanoparticle speciation in brain: distinguishing exogenous and endogenous Fe

Fe nanoparticle speciation was identified in olfactory bulb (OB) thin sections using high-resolution scanning/transmission electron microscopy (S/TEM) coupled with spectroscopic elemental mapping. A JEOL 2100 F field emission S/TEM operated at 200 kV with an analytic pole piece used for the OB sections and also to identify the as-synthesized Fe-nanoparticles collected on TEM grids (Ted Pella, Inc. Redding, CA) for comparison. OB thin sections were obtained after brains were extracted and placed in filtered 4% PFA for initial tissue fixation. After dissection (using the right hemisphere), the OB tissues were post-fixed in 2.5% glutaraldehyde using 0.1 M sodium phosphate buffer at 4 °C followed by fixation in EPON-Araldite epoxy resin and then embedded in epoxy and polymerized at 60 °C. All OB tissues were unstained to have a greater contrast of the Fe-nanoparticles with the cellular matrix. Tissue sections were cut to be ~ 70 nm using an ultramicrotome (Boeckeler Instruments, Inc., Tuscon, AZ) and were placed onto nickel formvar/carbon coated slot grids (Ted Pella Inc., Redding, CA) to stabilize the tissue during beam interaction. High-resolution images of Fe nanoparticles in the OBs were recorded with a Gatan Ultrascan 4 k CCD camera and data analysis and processing used Gatan Digital Micrograph software (Gatan, Inc.). The S/TEM analysis was coupled with spectroscopic elemental mapping of the Fe nanoparticles in the OB. A GATAN high angle annular dark field (HAADF) detector (Digiscan II) and an Oxfor Aztec EDS system from Oxford Instruments, Oxfordshire, United Kingdom were used. Energy dispersive spectroscopic analysis (EDS) was performed with a GATAN high angle annular dark field detector (HAADF), Digiscan II, Gatan 2000 Image Filter (GIF) with Oxford Aztec EDS software (Oxford Instruments, Oxfordshire, United Kingdom. All S/TEM images were acquired using an analytical probe with 0.17 nm.

Statistical analysis

Brain neurotransmitter levels and levels of Aβ and tau were analyzed using one way analysis of variance (ANOVA). Locomotor activity in five-minute time intervals and radial arm maze performance were analyzed with repeated measures ANOVA. NOR data were analyzed via one-way ANOVA separately for each session. Statistical analyses were conducted using JMP Pro 16.0 (SAS Institute Inc., Cary, NC, USA) stratified by sex based on known sex differences in response to Fe and of female bias in AD prevalence [1, 62–66]. P values ≤ 0.05 were considered statistically significant, while near significant values (p values ≤ 0.10) are also indicated. Outliers were first removed if confirmed using Grubb's test (GraphPad Software Inc., San Diego, CA). Outlier analysis was never iterative, i.e., only one sample removed per treatment group per endpoint. No outliers were removed from neurotransmitter analyses and so, acute neurotransmitter analyses included 3 brains per group per treatment and post-behavioral neurotransmitter analyses included 6 brains per group per sex. One female air mouse was excluded from the frontal cortex Aβ42 and Tau analyses and one female Fe mouse was excluded from the Hippocampal AB and Tau analyses. With the exception of one female Fe animal exclusion from session 2 of Novel Object Recognition, all other behavioral analyses utilized 6 animals per group per sex.

Kruskal Wallis non-parametric ANOVA was used to determine the significance of change amount of the 180 × 2 regions within the atlas for the axial, radial, and mean diffusion contrasts and volume of diffusion MRI metrics and volumes, likewise stratified by sex. The volume of each region was normalized by the total brain volume of each specimen prior to analysis. Secondly, an omnibus Kruskal Wallis test was performed with groups of male air versus female air versus male Fe versus female Fe to determine whether the commonly significantly changed regions for the sex stratified changed in the combined model. A posthoc Dunn's test with Sidak correction was used to identify the pairwise comparisons of groups that contributed most to any significant result. P values ≤ 0.05 were considered statistically significant. Eta^2 and Cohen's F were used to quantify strength of the effect size for significant results. The statical calculations of MRI data were done in MATLAB.

Prior to analysis of the MRI metrics and volumes, the values of the left and right structures were combined by summing volumes and performing the weighted mean on diffusion metrics. Parent structures are generated from all potential parents in the RCCF atlas. The volume of each region was normalized by the total brain volume. First, a 2-way ANOVA was carried out with interactions considering sex and iron exposure conditions. This was followed by a Kruskal–Wallis non-parametric ANOVA to consider each sex independently for the iron exposure condition. P values ≤ 0.05 were considered statistically significant. Eta^2 and Cohen's F [67] were used to quantify strength of the effect size for significant results. Using G* Power [68], with estimation of the minimal Cohen's F effect size needed to maintain statistical power of 0.8. In the 2-Way ANOVA with interaction testing, the estimated Cohen's F effect size needed to maintain sufficient power is 0.82, while for the stratified by sex Kruskal- Wallis Non-Parametric ANOVA, an effect size of 1.3 is needed to maintain the same power criteria. The statistical calculations of MRI data were done in MATLAB.

Results

Fe exposure concentrations

Mass Fe concentration averaged 109.5 ± 24.16 μg/m^3, and mean particle counts averaged 2.01E + 06 #/cm^3 across the 20 exposure sessions (Fig. 2A). The particle diameter remained in the nanoparticle range (43–52 nm) across the course of exposure (Fig. 2B). To compare deposition fractions in mice, a multiple-path particle dosimetry model (MPPD; Applied Research Associates, Inc. v3.04) was used, with respiratory parameters customized to B6C3F1 mouse with strain-specific functional residual capacity (FRC), upper respiratory tract (URT), respiratory rate (RR), and tidal volume (TV). Additionally, density of iron-oxides was set to an average 5.2 g/cm^3, based on the approximate density of singlet iron oxides (averaged between Fe_3O_4 and Fe_2O_3), with a median mass aerodynamic diameter (MMAD) of 0.04812 um as reported above. Using these parameters, estimates of particle deposition were modeled for comparison. The total modeled deposition fraction was 53.84%, with 33.48% depositing in the head, 15.61% depositing in the tracheobronchial region, and 4.7% depositing in the pulmonary region. Of the modeled pulmonary deposition, 16.53% deposited in the central respiratory airway and 3.83% deposited in the peripheral conducting respiratory airways.

Fe characterization, speciation and translocation to olfactory bulb

Nasal olfactory uptake of Fe nanoparticles and its speciation was assessed in olfactory bulb, the port of entry into brain and compared to Fe speciation on TEM grids from the inhalation chamber. The STEM analyses with corresponding elemental maps and electron diffraction of the as-synthesized Fe particles in Fig. 3 provide structural and compositional details for the grid collected Fe speciation from the exposure chamber which formed predominantly magnetite particles, i.e., Fe_3O_4. Most particles were spherical with polycrystalline domains although some euhedral crystals were recognized (Fig. 3 **A a**). Elemental mapping for Fe and O is shown in Fig. 3 **A b-c** which indicated that oxygen is evenly distributed through the bulk of the particles. At higher resolution,

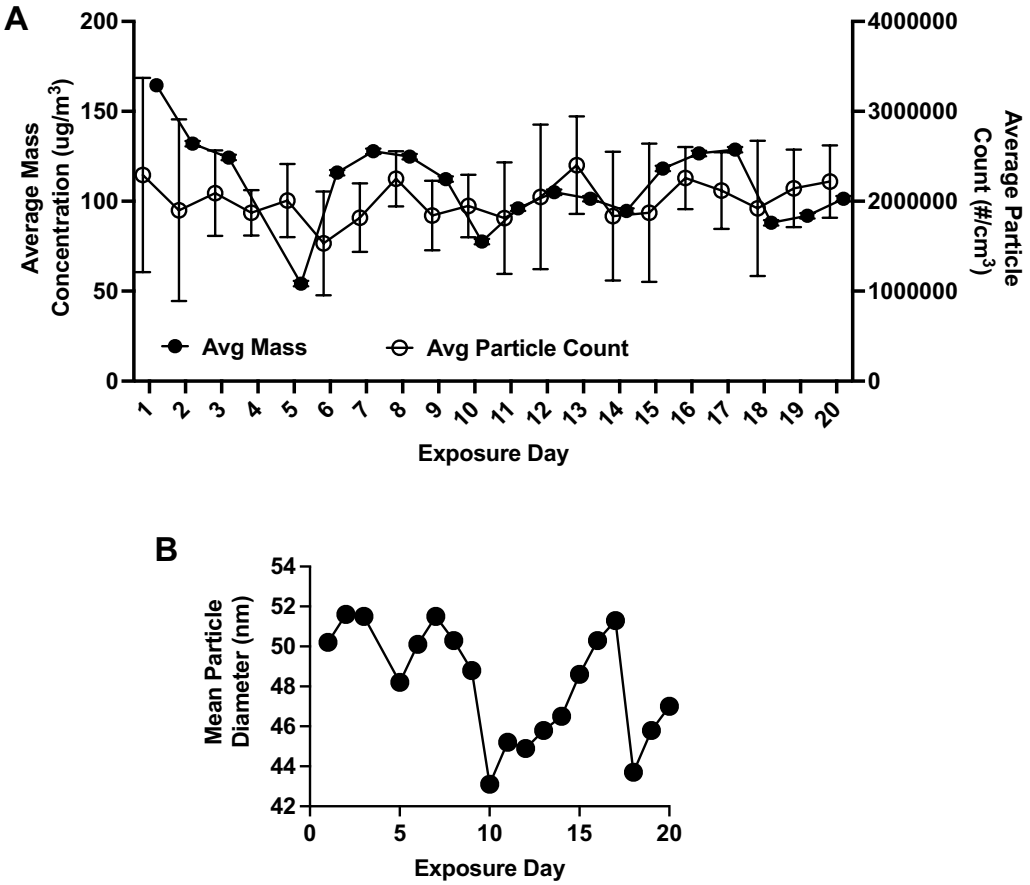

Fig. 2 **a** Mean ± standard deviation mass concentrations (μg/m^3) and particle counts (#/cm^3) of Fe oxide across the 20 exposure sessions. **b** Mean particle diameter (nm) across the 20 exposure sessions

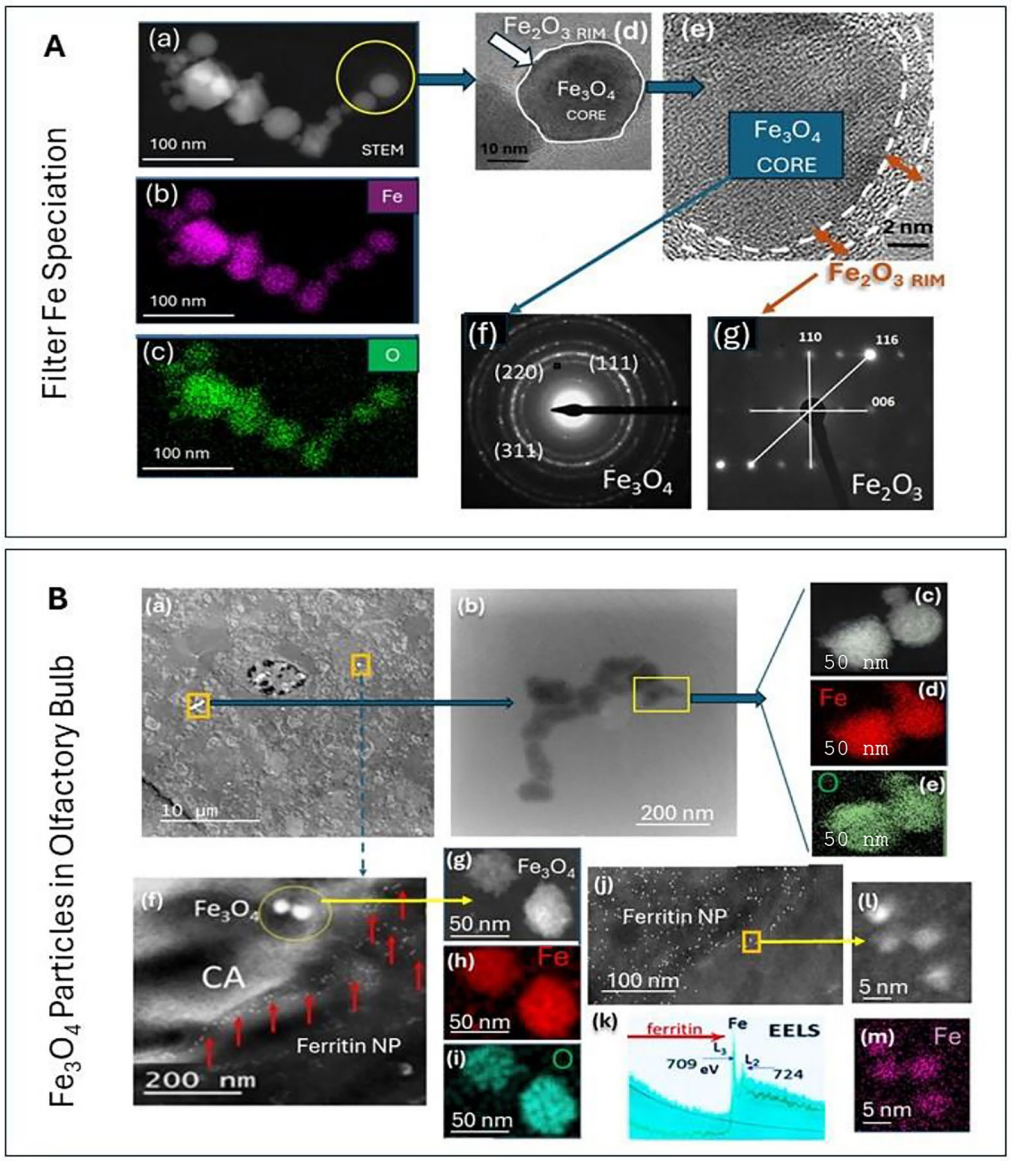

Fig. 3 Fe speciation is illustrated using STEM imaging. **Box A**: TEM Grid Fe Speciation. **a** STEM image shows Fe_3O_4 nanoparticle agglomerate with corresponding elemental maps for Fe (**b**) and O (**c**). High resolution STEM (**d–e**) shows polycrystalline Fe_3O_4 domains and a thin hematite (Fe_2O_3) rim approximately 1–2 nm wide with low density (red arrows). Electron diffraction patterns are illustrated for magnetite core (**f**) and hematite rim (**g**). **Box B**: Fe nanoparticles identified in olfactory bulb. **a** Two regions, marked with yellow square, where Fe particles translocated to olfactory bulb. A magnified view is shown in (**b**) and further magnified in (**c–e**) with corresponding elemental maps for Fe and O distribution. **f** STEM image illustrating the location of two isolated exogenous magnetite (Fe_3O_4) particles near a corpora amylacea body with copious endogenous Fe particle accumulation "ferritin NP". **g–l** further magnification of the Fe_3O_4 that show no Fe_2O_3 rims. **j**–**l** ferritin NP at higher magnification in the STEM images with corresponding elemental map for Fe (**m**). ELLS analysis of ferritin NP of the region marked in **j** with a yellow square. Correspondingly, Fe_3O_4 was detected in olfactory bulb from an Fe-exposed brain

the Fe_3O_4 spheres have a narrow band at the surface (Fig. 3 **A d-e**) that consists of hematite Fe_2O_3, a more oxidized Fe speciation that was further distinguished from the Fe_3O_4-rich core region of the Fe particles using electron diffraction (Fig. 3 **A f-g**).

The magnetite particles were also identified in the olfactory bulb after inhalation exposure (Fig. 3 **B a-m)** and found in close proximity to neurons and astrocytes and also next to corpora amylacea distinguished in the OB tissue regions using STEM imaging even in the unstained sections (Fig. 3 **B a**). Two examples of

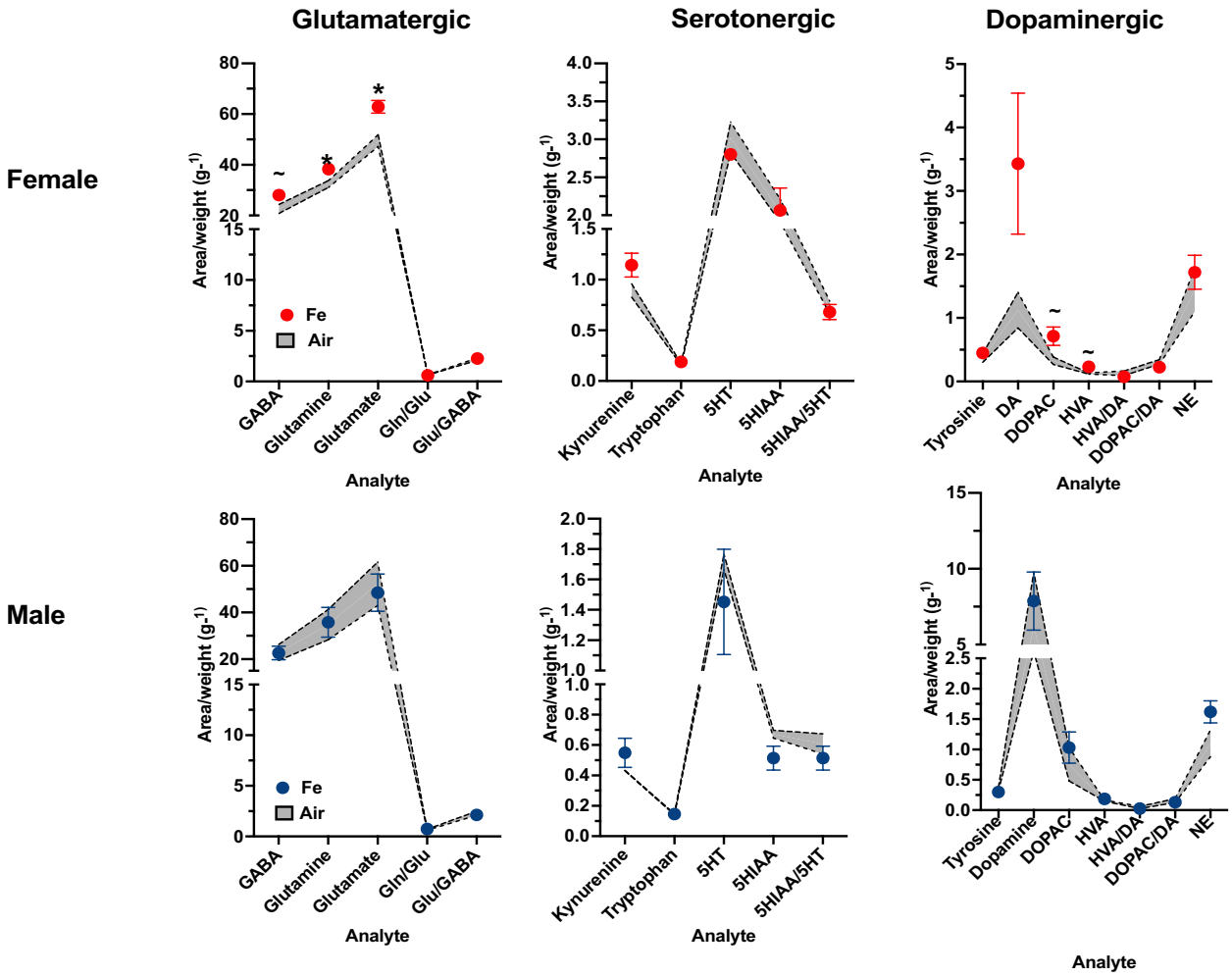

Fig. 4 Group mean ± SE levels of striatal glutamatergic, serotonergic and dopaminergic neurotransmitters (area/weight) (g^{-1}) in female (top row) and male mice (bottom row) exposed to filtered air (Air; gray shaded area) or Fe nanoparticles (Fe; symbols) measured two days post termination of exposure. GABA = gamma aminobutyric acid; Gln = glutamine; Glu = glutamate; Tyr = tyrosine; DA = dopamine; DOPAC = 3,4-dihydroxyphenylacetic acid; HVA = homovanillic acid; NE = norepinephrine; Kyn = kynurenine; Trp = tryptophan; 5HTP = 5-hydroxytryptophan; 5HT = serotonin; 5HIAA = 5-hydroxyindoleacetic acid. * statistically significant at $p \leq 0.05$; ~ p value ≤ 0.10

translocated Fe particles are indicated in Fig. 3 **B a,** and the larger Fe agglomerate magnified in Fig. 3 **B b-e,** with corresponding elemental maps for Fe and O. Results indicate that the magnetite (Fe_3O_4) particles that translocated to OB have the same chemical and crystalline structure as the spark-generated particles from the TEM grids. The surface rim of hematite (Fe_2O_3) around the magnetite core that was identified in the TEM grids sample was missing in the OB Fe particles which are characterized by a rougher surface layer potentially due to particle-tissue interaction and some bioprocessing of the particles that may cause partial dissolution along the surfaces (Fig. 3 **B c-e**). Many of the Fe particles in the OB were not agglomerated or had only one or two other particles nearby, as shown in Fig. 3 **B f-I** with corresponding elemental maps for Fe and O. Near the exogenous Fe particles were also copious amounts of biomineralized iron in the form of ferritin nanoparticles which were typically 3–12 nm in diameter that were not agglomerated. The ferritin are typically smaller in size compared to the exogenous Fe (Fig. 3 B f; j, l-m) and were identified using electron energy loss spectroscopy (EELS) analysis based on their FeL3 and FeL2 edges (Fig. 3 B d). Thus, Fe_3O_4 (magnetite) was detected on the grid post-exposure and Fe_3O_4 particles were likewise found in OB of Fe-exposed brain.

Brain neurotransmitter levels: Two days post-exposure

Levels of glutamatergic, serotonergic and dopaminergic classes of neurotransmitters were quantified in the striatum and cerebellum two days post termination of exposure.

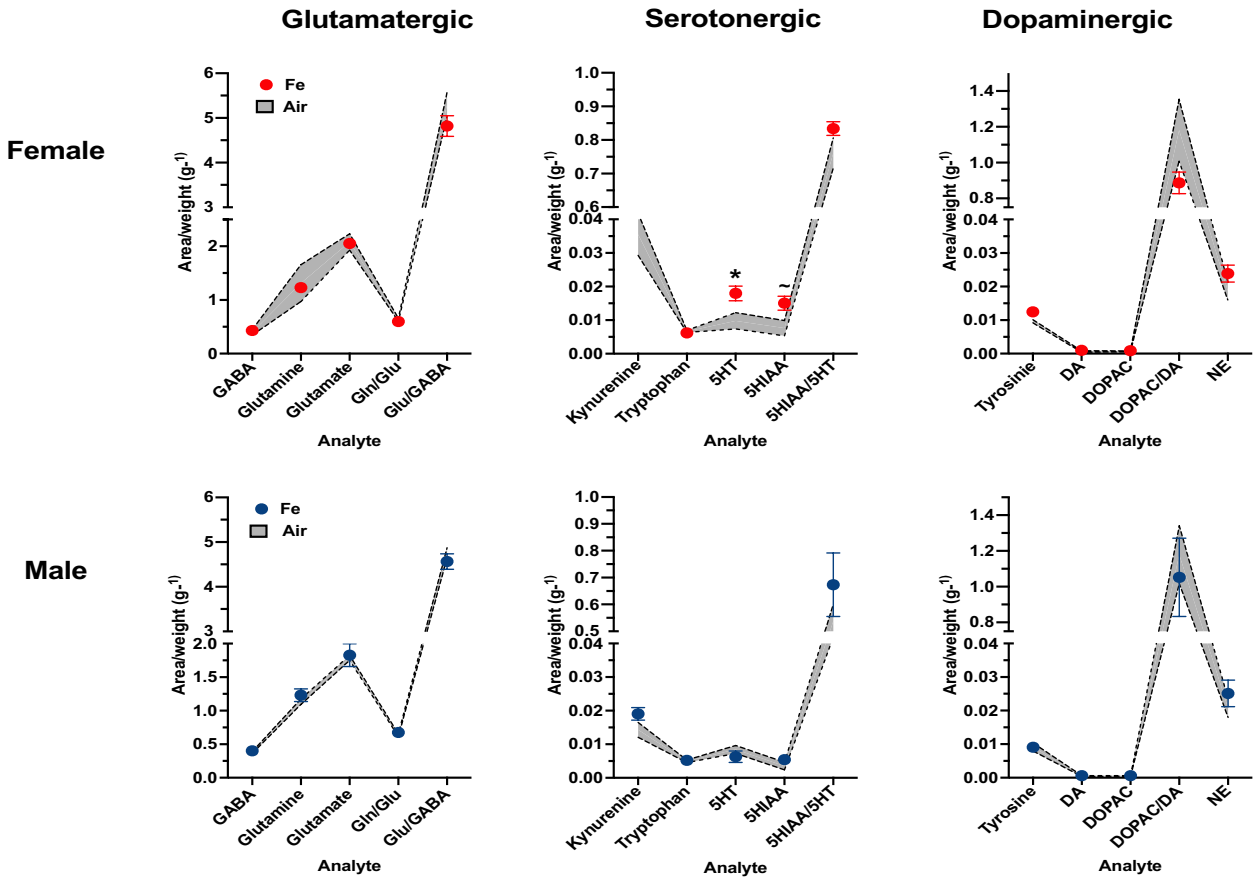

Fig. 5 Group mean ± standard error levels of glutamatergic, serotonergic and dopaminergic neurotransmitters (area/weight) (g^{-1}) in cerebellum of female (top row) and male mice (bottom row) exposed to filtered air (Air; gray shaded area) or Fe nanoparticles (Fe; symbols) measured two days post termination of exposure. (area/weight) (g^{-1}) in cerebellum of female mice (top row) and male mice (bottom row) exposed to filtered air (Air; gray shaded area) or Fe nanoparticles (Fe; symbols) measured two days post termination of exposure. GABA = gamma aminobutyric acid; Gln = glutamine; Glu = glutamate; Tyr = tyrosine; DA = dopamine; DOPAC = 3,4-Dihydroxyphenylacetic acid; HVA = homovanillic acid; NE = norepinephrine; Kyn = kynurenine; Trp = tryptophan; 5HTP = 5-hydroxytryptophan; 5HT = serotonin; 5HIAA = 5-hydroxyindoleacetic acid. * statistically significant at $p \leq 0.05$; ~ p value ≤ 0.10

Striatum – Fig. 4 shows striatal levels of neurotransmitters in Fe- and air-exposed females (top row) and males (bottom row). No significant differences in levels of any of the neurotransmitters within any of the three classes examined were found in response to inhaled Fe in males. In females, however, both glutamatergic and dopaminergic Fe-based changes were found. Specifically, within the glutamatergic system, significant Fe-related increases were found in levels of glutamine (Gln: + 19%, $F(1,4) = 7.88$, $p = 0.048$) and glutamate (Glu: + 29%, $F(1,4) = 15.38$, $p = 0.0172$), with a marginal increase in levels of GABA (+ 31%, $F(1,4) = 4.66$, $p = 0.097$). Marginal Fe-related increases were observed in levels of the dopamine metabolites DOPAC (+ 118%; $F(1,4) = 6.12$, $p = 0.069$) and HVA (+ 83%; $F(1,4) = 6.65$, $p = 0.061$).

Cerebellum—As in striatum, no significant changes were found in Fe-exposed male cerebellum in glutamatergic, dopaminergic or serotonergic neurotransmitter levels (Fig. 5). In females, significant increases were seen in levels of serotonin (5HT: + 83%, ($F(1,4) = 7.83$, $p = 0.049$) along with marginal increases in the 5HT metabolite 5-HIAA (+ 97%, ($F(1,4) = 7.47$, $p = 0.052$) within the serotonergic system.

Magnetic resonance histological imaging: Two days post-exposure

Magnetic resonance histological imaging of brains collected within 48 h of exposure revealed significant changes in mice exposed to Fe.

Sex + Exposure + Sex:Exposure Model

Table 1 shows the results of a 2-Way ANOVA with interaction model for diffusion tensor imaging, fractional

Table 1 Summary of MRI changes sex and exposure model

Structure	Statistical summary, Sex:Exposure	Male air vs Fe	Female air vs Fe
Diffusion tensor imaging changes			
Olfactory bulb	Mean: $p < 0.01$, Cohen's F 1.04	Mean: − 5.3%	Mean: 5.0%
	Radial: $p < 0.01$, Cohen's F 1.06	Radial: − 4.9%	Radial: 4.8%
	Axial: $p < 0.01$, Cohen's F 0.982	Axial: − 5.9%	Axial: 5.3%
Fractional anisotropy changes			
Structure	Statistical summary, Sex:Exposure	Male air vs Fe	Female air vs Fe
Posterior Amygdalar Nucleus	$p < 0.05$, Cohen's F 0.847	− 11.3%	5.2%
Voumetric changes			
Structure	Statistical summary, Sex:Exposure	Male air vs Fe	Female air vs Fe
Geniculate group, dorsal thalamus	$p < 0.01$, Cohen's F 0.948	3.5%	− 2.1%
Medial geniculate complex ventral part	$p < 0.05$, Cohen's F 0.919	5.1%	− 6.2%
Medial geniculate complex	$p < 0.05$, Cohen's F 0.851	2.7%	− 3.9%

Uncorrected *p*-values: negative (–) % change signifies that Air is larger and positive (+) % change signifies that Fe is larger. Volumetric findings were controlled by brain volume of each specimen, thus normalized volume. Sex is a significant for volumetric changes in the 2-Way ANOVA Models for these structures: Central Amygdalar Nucleus (Uncorrected $p < 0.01$, Cohen's F 1.37), Anteroventral Nucleus of Thalamus, (Uncorrected $p \ll 0.01$, Cohen's F 1.07), Prelimbic Area (Uncorrected $p < 0.01$, Cohen's F 0.876), Orbital Area (Uncorrected $p < 0.05$, Cohen's F 0.888), Superior Colliculus-Sensory Related (Uncorrected $p < 0.05$, Cohen's F 0.887), and Ventral Posteromedial Nucleus of the Thalamus (Uncorrected $p < 0.05$ Cohen's F 1.00). There were no structures with significant changes in diffusion tensor metrics or normalized volume related to exposure alone

anisotropy and volumetric changes providing a high-level overview of changes.

Diffusion tensor imaging changes

As shown in Table 1**,** olfactory bulb was impacted by Fe inhalation, with significant mean, radial and axial diffusivity contrasts for the sex:exposure interaction. The male and female response was in the opposite directions, with increases in Fe-exposed females in mean, radial and axial diffusivity, and reductions in mean, radial and axial diffusivity in olfactory bulb in Fe-exposed males. Post hoc testing (Tukey–Kramer HSD method via multcompare in MATLAB) indicated that for mean, radial and axial diffusivity, the female Fe versus male Fe was the most significant pairwise comparison set ($p < 0.1$).

Fractional anisotropy

Analyses revealed one structure, posterior amygdalar nucleus, that was significantly changed for the sex:exposure interaction. Male mice exhibited a decrease in the fractional anisotropy following Fe exposure (− 11.3%), while female mice showed an increase in response to Fe exposure (+ 5.2%).

Volume changes

There were significant changes in multiple components of the geniculate complex (most child to parent structure ordering: medial geniculate complex, ventral part; medial geniculate complex; geniculate group, dorsal thalamus). Specifically, male mice had increases in the volume (+ 5.1%, + 2.7%, and + 3.5%) with Fe exposure, while female mice showed decreases in volume (− 6.2%, − 3.9%, − 2.1%) in response to Fe exposure.

Stratified by sex: changes observed two-days post-exposure

Table 2 shows the results of stratified by sex Kruskal Wallis non-parametric ANOVAs indicating significant diffusion tensor imaging, fractional anisotropy and volumetric changes.

Diffusion tensor imaging changes

Olfactory bulb was significantly influenced by Fe in both female and male mice, but again in opposite directions (Fig. 6). Additional analyses revealed sex-dependent changes in olfactory bulb diffusivity consistent with increased myelin damage and axonal loss. Specifically, the mean male response to Fe exposure (axial: 0.348 ± 0.0171 $10^{-3} \times mm^2/s$, radial: 0.270 ± 0.0105 $10^{-3} \times mm^2/s$, mean: 0.296 ± 0.0127 $10^{-3} \times mm^2/s$) was lower than that than of the mean female response to Fe exposure (axial: 0.373 ± 0.00649 $10^{-3} \times mm^2/s$, radial: $0.286 \pm 0.0.0360$ $10^{-3} \times mm^2/s$, mean: 0.315 ± 0.00441 $10^{-3} \times mm^2/s$), assisting in explaining why in the post hoc analysis of the overall 2-Way ANOVA model, this pairwise comparison was also the most changed, i.e., the most different pairing.

Additional significant changes in the diffusion tensor metrics were unique to each sex. For male mice, there were significant reductions in olfactory areas (mean: − 4.2%, axial − 4.8%), and hippocampal commissures (radial: − 4.4%), while for female mice, there were

Table 2 Summary of MRI changes stratified by sex

Male		Female	
Structure	**Air vs Fe**	**Structure**	**Air vs Fe**
Diffusion tensor imaging changes			
+ Olfactory Bulb	Mean: − 5.3%	+ Olfactory Bulb	Mean: 5.0%
	Radial: − 4.9%		Radial: 4.8%
	Axial: − 5.9%		Axial: 5.3%
Olfactory areas	Mean: − 4.2%	Anterior olfactory nucleus	Axial: 5.4%
	Axial: -4.8%		
Hippocampal commissures	Radial: − 4.4%		
Fractional anisotropy changes			
+ Posterior amygdalar nucleus	− 11.3%		
Hypoglossal nucleus	− 10.7%		
Pretectal region	− 10.3%		
Medial preoptic nucleus	8.9%		
Nucleus accumbens	7.9%		
Basomedial amygdalar nucleus	− 7.0%		
Subicular region	− 6.6%		
Cortical amygdalar Zones	− 6.4%		
Fimbria	− 6.1%		
Cranial nerves	− 5.6%		
Trigeminal nerve	− 5.4%		
Striatum ventral region	4.1%		
CA1	− 2.4%		
Volumetric changes			
Substantia Nigra Compact part	8.0%	+ Medial geniculate complex, ventral part	− 6.2%
Trigeminal nerve	− 6.0%	Vestibulocerebellar Nucleus	5.5%
Midline group of the dorsal thalamus	5.2%	Lateral amygdalar nucleus	− 3.6%
Optic tract and Chiasm	− 4.7%	Medulla sensory related	2.4%
Posterior complex of the thalamus	4.1%		
Spinal vestibular nucleus	3.6%		
+ Geniculate group, dorsal thalamus	3.5%		
Epithalamus	− 3.0%		
Bed nuclei of the stria terminalis	− 2.1%		

+ Structures which appeared significant in the 2-Way ANOVA analysis, considering sex and exposure together. For all entries, uncorrected *p*-values is < 0.05 and estimated Cohen's F is 1.73. Negative (−) % change signifies that Air is larger and positive (+) % change signifies that Fe is larger. Volumetric findings were controlled by brain volume of each specimen, thus is normalized volume

significant increases in the anterior olfactory nucleus (axial: + 5.4%).

Fractional anisotropy

Alterations in fractional anisotropy in the MRI assessment were male-specific (Table 2). Fe-exposed males showed significant reductions in fractional anisotrophy (FA) in posterior amygdalar nucleus (− 11.3%), hypoglossal nucleus (− 10.7%), pretectal region (− 10.3%), basal amygdalar nucleus (− 7.0%), subicular regiona (− 6.6%), cortical amygdalar zones (− 6.4%), fimbria (− 6.1%), cranial nerves (− 5.6%), trigeminal nerve (− 5.4%), and CA1 (− 2.4%). Increases in FA in Fe-exposed males were seen in medial preoptic nucleus (+ 8.9%), nucleus accumbens (+ 7.9%), and ventral part of striatum (+ 4.1%).**Volumetric Changes**—As shown in Table 2, male Fe-exposed mice showed a significant increase in the normalized volume of the substantia nigra compact part (+ 8.0%), midline group of the dorsal thalamus (+ 5.2%), the posterior complex of the thalamus (+ 4.1%), the spinal vestibular nucleus (+ 3.6%), and the geniculate group, dorsal thalamus (+ 3.5%). Males concurrently exhibited significant volumetric reductions in the trigeminal nerve (− 6.0%), the optic tract and chiasm (− 4.7%), epithalamus (− 3.0%), and of the bed nuclei of the stria terminalis (− 2.1%).

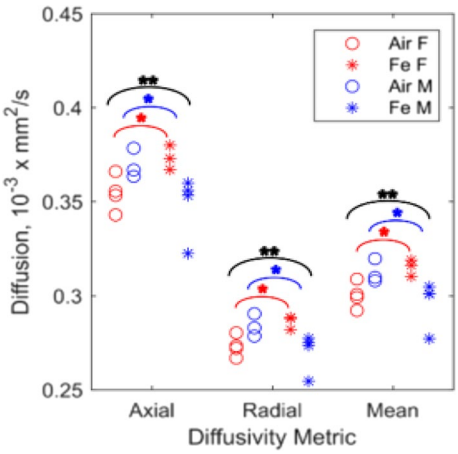

Fig. 6 Individual specimen diffusivity values ($10^{-3} \times mm^2/s$) in olfactory bulb of male mice exposed to filtered air (blue circles) or Fe nanoparticles (blue asterisks) and female mice exposed to filtered air (red circles) or Fe nanoparticles (red asterisks) as assessed in dMRI from specimen perfused two days post termination of exposure. * statistically significant at uncorrected $p \leq 0.05$ for each diffusivity value grouping. ** statistically significant at uncorrected $p \leq 0.01$ for each diffusivity value grouping. Black is significance determined by the 2-Way ANOVA with interactions analysis. Red (female) and Blue (male) indicates significance as determined by the stratified Kruskal Wallis non-parametric ANOVAs

Females showed a significant 5.5% increase in the normalized volume of the vestibulocerebellar nucleus with corresponding significant reductions in volume which were largest in the ventral medial geniculate complex (−6.2%, Table 2), but also showed significant reductions in the lateral amygdala nucleus (−3.6%) and the sensory related portions of the medulla (−2.4%).

Aβ42 and Tau: 6 months post-exposure

As measured approximately 6 months post inhaled Fe exposure, neither protein levels of pS199 tau, total tau, and Aβ42 concentrations in frontal cortex or hippocampus were affected in male mice (Fig. 7). In contrast, Fe-exposed female mice exhibited significantly higher concentrations in frontal cortex of pS199 tau ($t=2.76$, $p=0.02$) and of total tau ($t=3.63$, $p=0.008$), but similar concentrations of Aβ42 ($t=0.99$, $p=0.35$) as compared to air-exposed controls. Fe-exposed female mice also exhibited significantly higher hippocampal concentrations of total tau ($t=2.57$, $p=0.028$) than did air-exposed controls, but showed similar concentrations of hippocampal pS199 tau ($t=1.50$, $p=0.17$) and Aβ42 ($t=-1.23$, $p=0.25$).

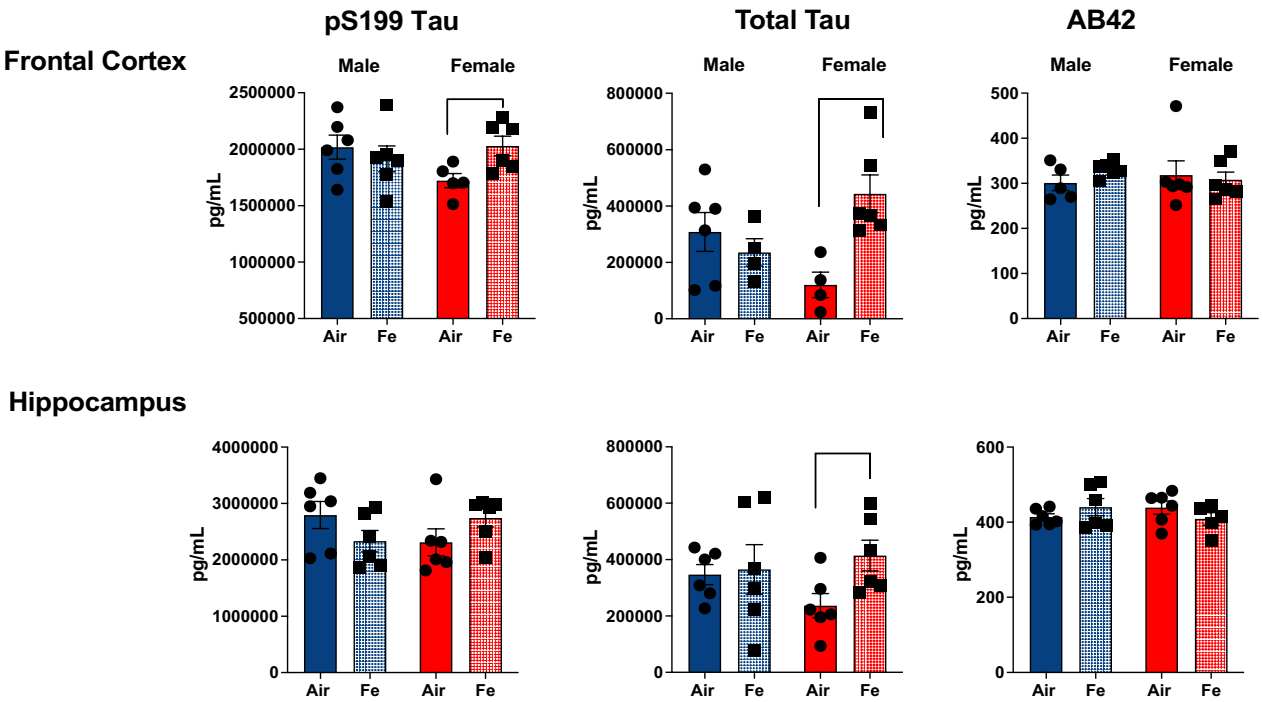

Fig. 7 Group mean ± standard error levels of phosphorylated tau (left column), total tau (middle column) and Aβ42 (right column) (pg/mL) in frontal cortex (top row) and hippocampus (bottom row) of male (blue) and female (red) mice exposed to filtered air (Air) or Fe nanoparticles (Fe). * indicates statistically significant at $p \leq 0.05$

Behavioral changes post-exposure

Locomotor activity levels

Fe-exposed males showed no significant differences from air-exposed males in any measures of locomotor activity levels: ambulatory distance, ambulatory episode, ambulatory time, jump counts, jump time, rest time, stereotypic counts, stereotypic time, vertical counts, or vertical time (Supplementary Fig. 1). Similarly, females, regardless of treatment group, performed equivalently across all measures of locomotor behavior.

Novel object recognition

In session 1 of NOR, mice, regardless of sex and treatment, spent equivalent amounts of time with both the left- and the right-placed object as determined by comparing time spent with left or right object vs. half of total interaction time (Fig. 8), confirming an absence of spatial or activity level bias that could influence results in session 2 determination of the NOR recognition index. Recognition index in session 2, calculated as time spent with the novel object divided by total time spent with both objects averaged 58% and 68%, respectively, for male and female air control mice, consistent with recognition of a novel stimulus. This recognition index was not influenced by Fe exposure in male mice. However, Fe-exposed female mice displayed a 31% significantly lower recognition index than their air-exposed controls (t=-5.19, p=0.0007).

Radial arm maze

Radial arm maze performance was assessed over 3 sessions in females and 5 sessions in males (Fig. 9). No significant effects of Fe on percent errors were seen in male mice over the course of the 5 sessions of testing, with both groups showing chance levels of accuracy in session 1 and slight declines thereafter. In contrast, while chance

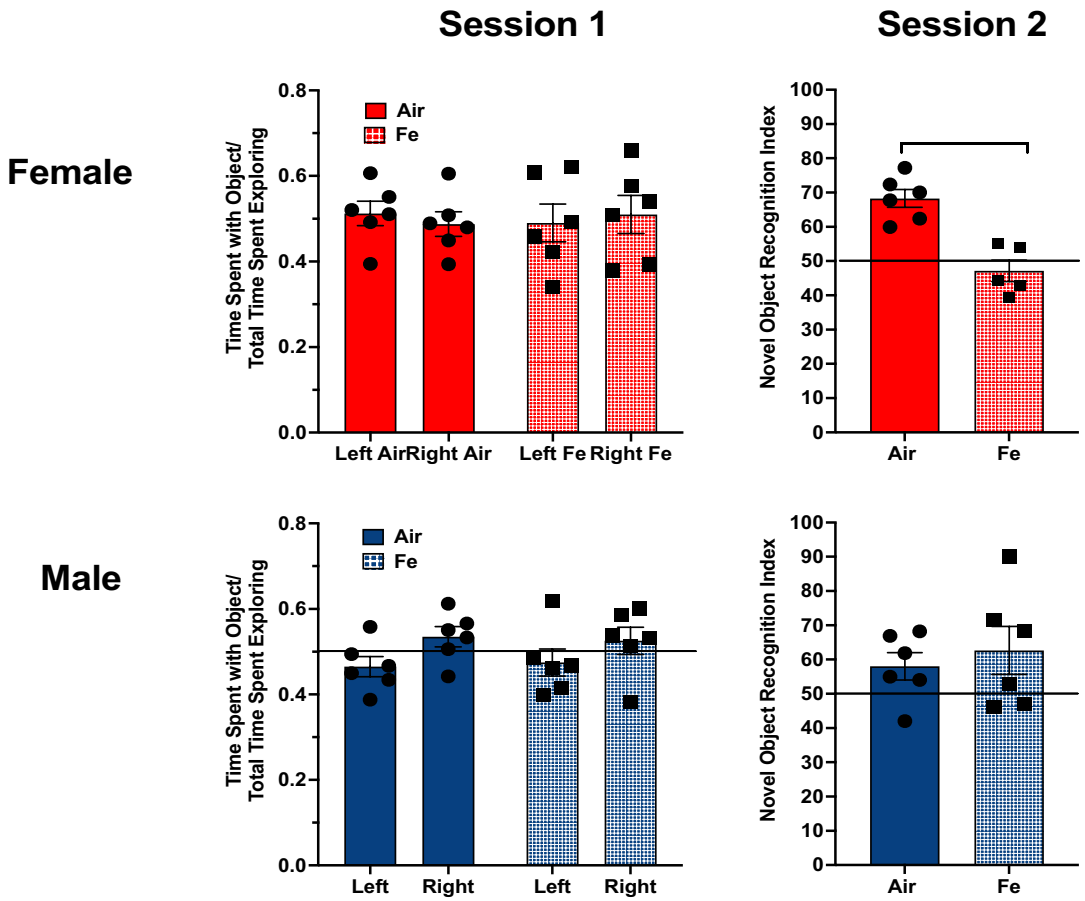

Fig. 8 Left Column: Group mean ± SE levels of time spent with object/total time spent exploring in session one (left column) of left and right objects in females (top left) and males (bottom left) exposed to filtered air (Air) or to Fe nanoparticles (Fe). Right Column: novel object recognition index in NOR session 2 for males (blue) and females (red) exposed to filtered air (Air) or to Fe nanoparticles (Fe). * indicates statistically significantly different from Air at $p \leq 0.05$

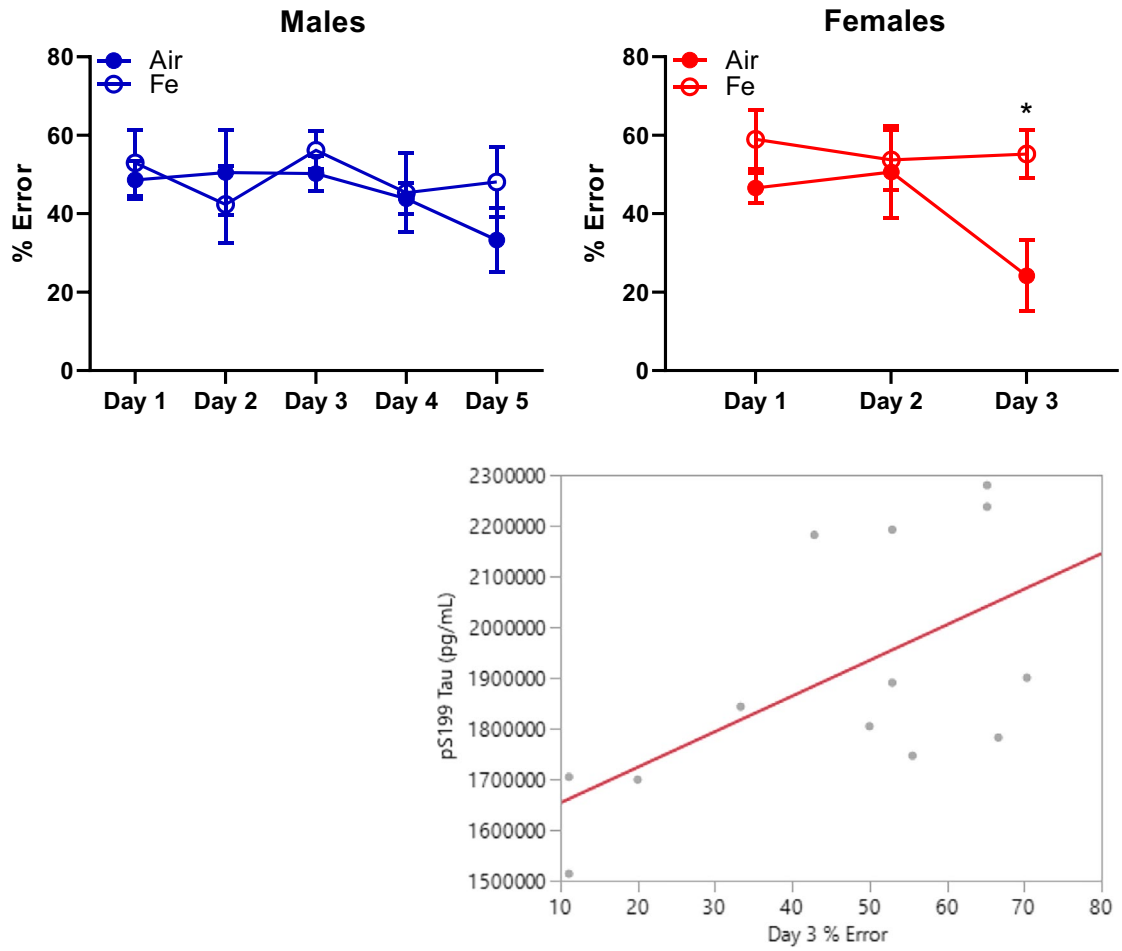

Fig. 9 Top row: Group mean ± standard error of percent errors on the RAM in males (left) and females (right) exposed to filtered air (closed circles) or Fe nanoparticles (open circles) across days of measurement. * indicates statistically significantly different from Air at $p \leq 0.05$. Bottom row: Correlation of frontal cortex phosphorylated tau levels (pg/mL) with percent errors during session 3 of RAM in female mice

levels of errors were also seen in female mice in sessions 1 and 2, levels of errors in female control mice dropped in session 3 by almost 30%, whereas no such change was found in Fe-exposed females, resulting in a marginally significant interaction in the repeated measures analysis (time x treatment ($F(2, 9) = 0.060$), with a significant day 3 reduction confirmed in a subsequent post-hoc t-test ($t = 2.86$, $p = 0.017$). Notably, levels of percent errors in Session 3 in females (Fig. 9, bottom), including both air- and Fe-exposed mice, were significantly correlated with hippocampal levels of phosphorylated tau ($r^2 = 0.37$; $F(1,11) = 6.44$, $p = 0.0275$).

Post-behavior neurotransmitter changes

Changes in striatal and cerebellar neurotransmitter levels were examined post behavioral testing in mice that underwent behavioral assessments.

Striatum

In contrast to effects seen 48 h post exposure, significant Fe-induced changes in striatal neurotransmitters post behavioral testing were seen only in males (Fig. 10). In Fe-exposed females, the only change seen was a marginal (8%) increase in excitotoxicity (glutamate/GABA; $F(1,10) = 3.29$, $p = 0.0998$). In contrast, changes in all three classes of neurotransmitters were now evident in males. Effects within the class of glutamatergic neurotransmitters included a significant 19% increase in levels of GABA ($F(1,10) = 6.25$, $p = 0.031$), a 40% marginal increase in levels of glutamine ($F(1,10) = 4.59$, $p = 0.058$) and a 22% marginal increase in glutamate ($F(1,10) = 4.4$, $p = 0.062$). Changes seen within the class of serotonergic neurotransmitters in Fe-exposed male striatum included an 84% marginal increase in kynurenine ($F(1,10) = 4.71$, $p = 0.0552$), as well as a 32% significant reduction in levels of serotonin ($F(1,10) = 18.32$, $p = 0.0016$). Change also occurred

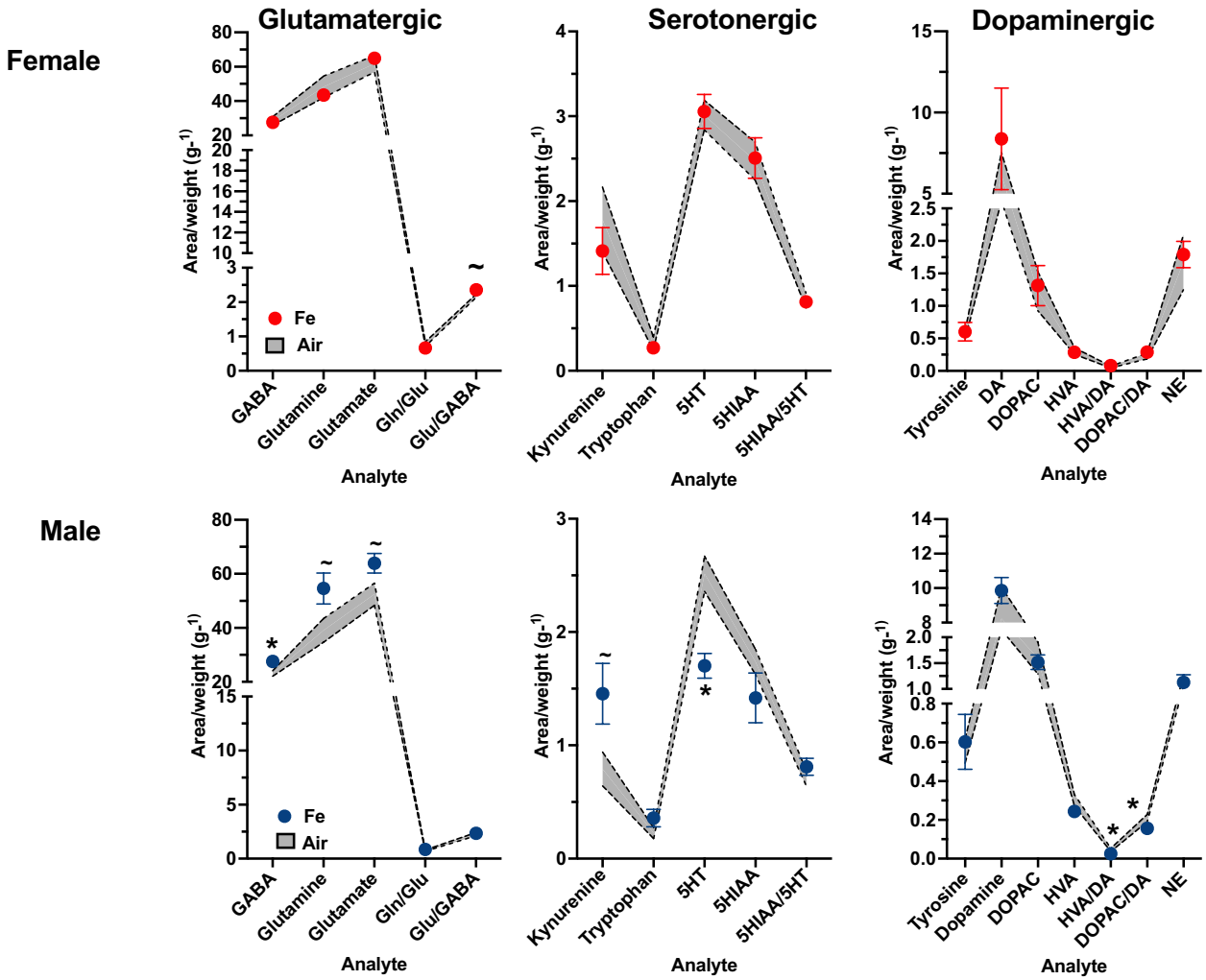

Fig. 10 Group mean ± standard error levels of glutamatergic, serotonergic and dopaminergic neurotransmitters (area/weight) (g^{-1}) in striatum of female (top row) and male mice (bottom row) exposed to filtered air (Air; gray shaded area) or Fe nanoparticles (Fe; symbols) measured after behavioral testing. GABA = gamma aminobutyric acid; Gln = glutamine; Glu = glutamate; Tyr = tyrosine; DA = dopamine; DOPAC = 3,4-Dihydroxyphenylacetic acid; HVA = homovanillic acid; NE = norepinephrine; Kyn = kynurenine; Trp = tryptophan; 5HTP = 5-hydroxytryptophan; 5HT = serotonin; 5HIAA = 5-hydroxyindoleacetic acid. * indicates statistically significant at $p \leq 0.05$; ~ indicates p value ≤ 0.10

in response to Fe within the class of dopaminergic neurotransmitters, specifically in reduced dopamine turnover, with a 44% significant reduction in the ratio of HVA/DA ($F(1,10) = 5.2$, $p = 0.046$) as well as a significant 25% reduction in the ratio of DOPAC/DA ($F(1,10) = 5.4$, $p = 0.043$).

Cerebellum

Post behavior changes in cerebellar neurotransmitter function (Fig. 11) were more limited. In females, Fe-induced changes were limited to a marginal 17% increase in levels of glutathione ($F(1,12) = 4.1$, $p = 0.066$). In males exposed to Fe, a significant 28% increase in levels of serotonin turnover were observed ($F(1,12) = 5.69$, $p = 0.035$) in conjunction with a marginal 20% increase in dopamine turnover (DOPAC/DA; $F(1,12) = 3.52$, $p = 0.085$).

Trans-sulfuration markers

Changes in levels of markers within the trans-sulfuration pathway, specifically methionine, homo-cysteine, cysteine and glutathione, were measured in both striatum and cerebellum at 2 days post-exposure (labeled Pre) and after behavioral testing (labeled Post) and are depicted in Fig. 12. In striatum, females evidenced significant increases in glutathione even at 2 days post

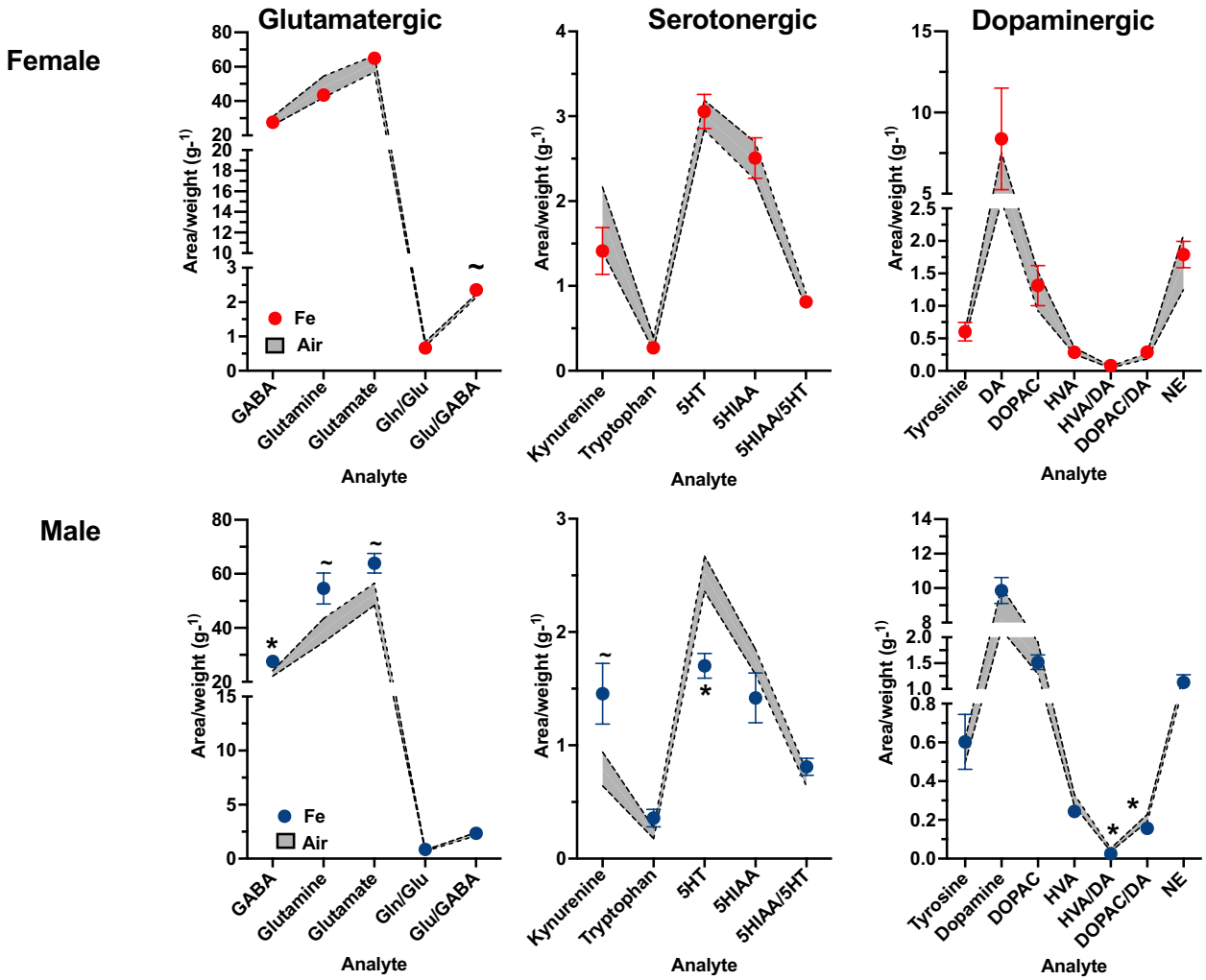

Fig. 11 Group mean ± standard error levels of glutamatergic, serotonergic and dopaminergic neurotransmitters (area/weight) (g^{-1}) in cerebellum of female (top row) and male mice (bottom row) exposed to filtered air (Air; gray shaded area) or Fe nanoparticles (Fe; symbols) measured after behavioral testing. (area/weight) (g^{-1}) in cerebellum of female mice (top row) and male mice (bottom row) exposed to filtered air (Air; gray shaded area) or Fe nanoparticles (Fe; symbols) measured two days post termination of exposure. GABA = gamma aminobutyric acid; Gln = glutamine; Glu = glutamate; Tyr = tyrosine; DA = dopamine; DOPAC = 3,4-Dihydroxyphenylacetic acid; HVA = homovanillic acid; NE = norepinephrine; Kyn = kynurenine; Trp = tryptophan; 5HTP = 5-hydroxytryptophan; 5HT = serotonin; 5HIAA = 5-hydroxyindoleacetic acid. * indicates statistically significant at $p \leq 0.05$; ~ indicates p value ≤ 0.10

Fe exposure (GSH: + 23%, $F(1,4) = 10.17$, $p = 0.0332$), with levels remaining elevated albeit not significantly when measured post behavioral testing. Notably, males showed a marked 44% significant increase in glutathione ($F(1,10) = 6.65$, $p = 0.028$) but this was not evident until post behavioral testing, and was accompanied by a significant 31% increase in levels of cysteine ($F(1,10) = 10.07$, $p = 0.0099$). Some evidence of a delayed increase in glutathione was also seen in females in cerebellum ($F(1,12) = 4.098$, $p = 0.066$).

Discussion

Based on the accumulating evidence linking both AP exposure [22, 23] and elevated brain Fe [1, 2] concentrations with risk for neurodegenerative diseases and disorders, the current study sought to examine in a mouse model the hypothesis that inhaled Fe, as would occur through AP exposures, would reach brain and would reproduce features of such diseases and disorders, and do so in a sex-dependent manner. Consistent with these hypotheses, speciation analyses of TEM grids from the exposure chambers confirmed

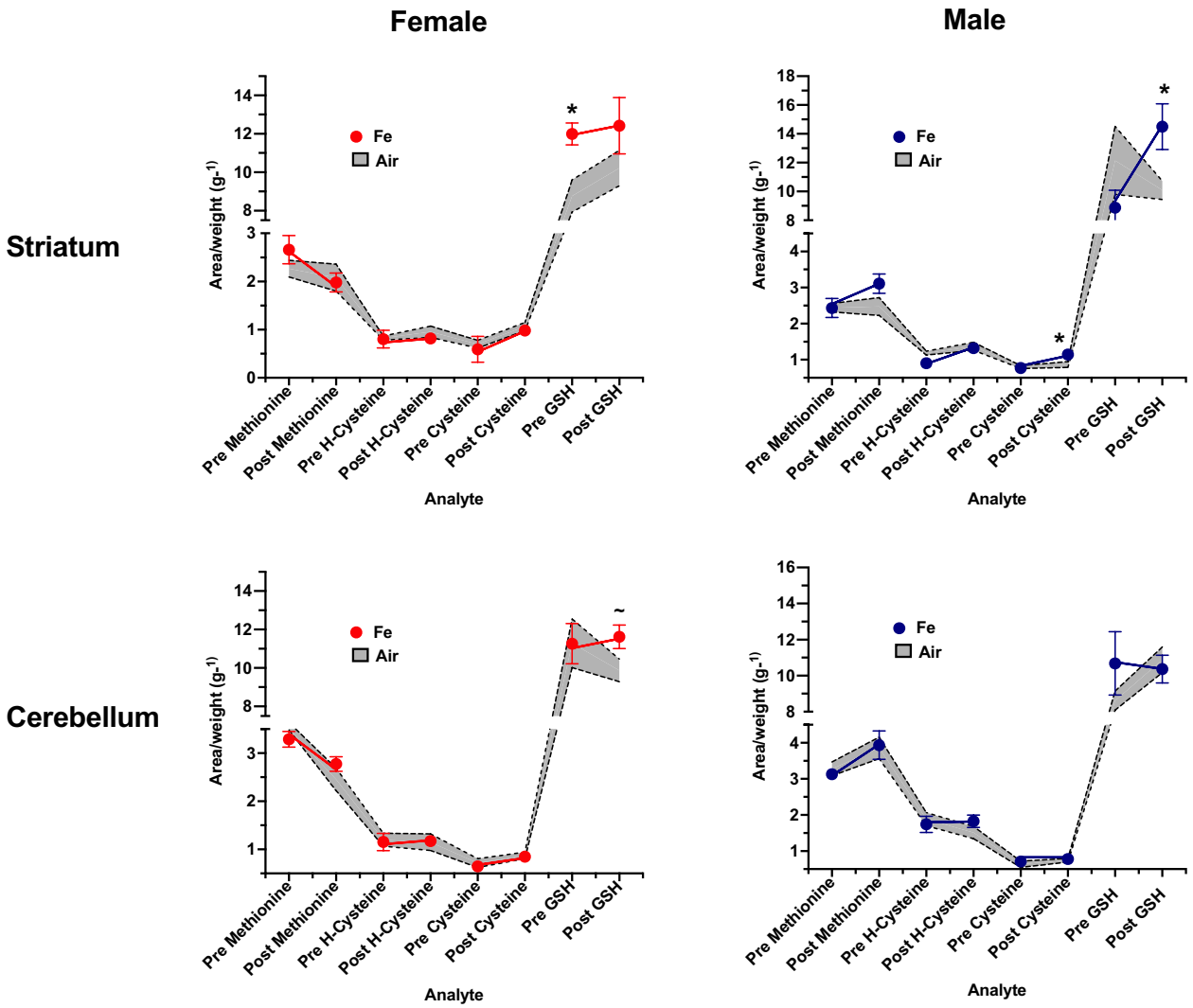

Fig. 12 Group mean ± standard error levels of striatal (top row) and cerebellar (bottom row) transulfuration markers of females (left column) and males (right column) exposed to filtered air (gray shaded area) or to Fe measure at 2 days post exposure (pre) and following behavioral testing (post) including methionine, h-cysteine, cysteine and glutathione (GSH). * statistically significant at $p \leq 0.05$; ~ p value ≤ 0.10

the presence of spark-generated, exogenous magnetite which was likewise seen in olfactory bulb, the initial port of entry into brain following nasal olfactory uptake in response to Fe inhalation, confirming the uptake of exogenous Fe. Additionally, characteristics of neurodegenerative diseases and disorders occurred in response to Fe inhalation and differed notably by sex. Specifically, females evidenced characteristics of AD that included increased levels of phosphorylated tau in frontal cortex and total tau in both frontal cortex and hippocampus, increases in olfactory bulb diffusivity potentially indicative of myelin damage and/or axonal loss, and Fe-exposed impaired memory, as assessed using both using a novel object recognition paradigm and a radial arm maze paradigm, with the latter impairments significantly correlated with levels of frontal cortical phosphorylated tau. In contrast, the profile of consequences in males showed characteristics associated with PD that included increases in volume of the substantia nigra pars compacta concurrently with reductions in the volume of the trigeminal nerve, and in mean, radial and axial diffusivity in olfactory bulb and hippocampus and altered fractional anisotropy changes in multiple subcortical structures.

S/TEM analysis coupled with EDS confirmed the presence of magnetite in mouse olfactory bulb following Fe inhalation based on their structural and crystalline similarity to the spark generated Fe nanoparticles

produced and collected on TEM grids (Fig. 3). Such findings are consistent with nasal olfactory uptake of elemental AP particles and salts in both rats and humans [69], including Fe, Mn, Cd, Ni, Hg, Al, Co, Zn, and Cu [69–74], through translocation across olfactory epithelium by olfactory neuronal cells along neuronal tracts, followed by transportation into olfactory bulb, and movement to other brain regions [18]. Sensory nerves in the upper and lower respiratory tract, e.g., the trigeminal ganglion or the vagal nerve, can also translocate particles [75] that reach the brain [18].

That Fe-contaminated AP may be a source of excess brain Fe is suggested by two studies. In one, an abundant presence of magnetite (Fe^{2+}/Fe^{3+} iron oxide) nanoparticles approximately 10–150 nm in size, interpreted as being consistent with an exogenous rather than endogenous source of Fe formation based on crystal morphologies that pinpoint to high temperature formational mechanisms such as during coal combustion, was identified in frontal cortex of brains from AD patients [76]. Additionally, a recent report found an accumulation of ambient black carbon particles (a component of air pollution particulate matter) in thalamus, prefrontal cortex and olfactory bulb and hippocampus in post-mortem brains from individuals with neuropathologically confirmed Alzheimer's disease [77]. Increases in Fe have been reported in brain and nerves of mice in other studies after inhalation exposures of Fe nanoparticles [78].

The olfactory route of exposure/uptake of Fe is of particular interest to reports defining the staging of neurodegenerative disorders, including AD and PD, as olfactory bulb is found as an early site of change in both [79, 80]. In the current study, Fe-based changes in olfactory bulb diffusivity were found in both sexes, with reductions in diffusivity in males, but increases in females, findings suggesting potentially different trajectories of neuropathology by sex, as has previously been noted [81]. While it is not yet clear how olfactory bulb changes translate into neuropathological features, such findings could suggest potential myelin abnormalities and/or axonal changes [82]. Interestingly, in our prior studies of developmental air pollution exposures, hypermyelination of the corpus callosum occurred in both sexes following gestational exposures, and correlated in females with Fe inclusions and axonal changes including thick myelin sheaths with "holes" indicative of damage [83, 84], while in males, postnatal exposures resulted in hypomyelination of the corpus callosum [85]. Future research is needed to associate these AP related myelin changes with MR diffusivity measures.

In terms of disease staging, Braak staging of PD suggests a pathogen entering the brain via the nasal route or trigeminal nerve or via the vagal nerve as initial sites of pathology [79, 86], consistent with nanoparticle routes to brain, with studies reporting olfactory bulb as an area that accumulates alpha-synuclein aggregates, a hallmark of PD. Of additional support is a study that examined metal concentrations and distributions in the human post-mortem brain in PD and found elevated Fe in the PD olfactory bulb [87]. In the case of AD, the unfolded protein response that leads to upregulation of beta-amyloid and tau production, hallmark features of AD, is found throughout the olfactory system, including Braak stages 0 and 1 [88, 89]. The olfactory bulb pathology indicated by increased diffusivity in MRI analyses in female Fe-exposed mice is consistent with the well documented involvement of olfactory bulb in dementia and AD, and indicative of changes to white matter microstructure. In accord with these findings, olfactory loss is considered to be a component of the long prodromal phase of AD as well as in PD [90].

Females showed several additional characteristic features of AD following Fe inhalation, including volumetric reductions in regions likewise implicated in AD and that include structural connections with olfactory system [91]. For example, reductions in amygdala volume have long been recognized in AD [92] and have been found to be of greater magnitude in lateral amygdala [93], the specific nucleus in which volumetric reductions were seen in Fe-exposed female brain in this study. It is notable that hippocampus and amygdala show early involvement in AD and receive projections from the olfactory bulb [94]. In contrast to these regions, increases in size of the vestibulocerebellar nucleus (flocculus) were concurrently found in female Fe-exposed brains. While prior studies have cited involvement of cerebellum in AD, these were seen as reductions [95, 96] as determined in individuals with diagnosed dementia. One potential basis for this increase could be an early compensatory plasticity. While compensatory mechanisms in AD have been proposed [97], the earliest changes in AD and possible compensatory processes have yet to be established. As with some other outcomes, studies of the time course of the consequences of Fe would provide important mechanistic information.

Females exposed to Fe likewise showed evidence of impaired memory, with these impairments correlated with increased levels of phosphorylated tau in frontal cortex. A hallmark of AD is the neuropathological misfolding and aggregation of two brain proteins, amyloid β (Aβ) and tau. Correlations between elevation of brain Fe and formation of neurofibrillary tangles have been reported [98]. Fe interacts with tau: Fe^{3+} can induce aggregation of hyperphosphorylated tau, while reduction of Fe^{3+} to Fe^{2+} reverses the effect, as shown

in hyperphosphorylated tau obtained from AD brains [98, 99]. The reduction of Fe^{3+} to Fe^{2+} can solubilize iron since Fe^{2+} can be present and transported in ionic form and hence, be mobilized. Another way to reduce Fe^{3+} to Fe^{2+} is to reduce the common Fe_2O_3 (hematite) to Fe_3O_4 (magnetite) which does not mobilize or remove Fe from the tissue regions. The correlation of frontal cortex phosphorylated tau levels with impaired memory is of particular interest given the reported role of tau in cognitive deficits in AD [100, 101]. It has been suggested that entorhinal cortex tau accumulation underlies hippocampal activation and memory loss over time [102], while cerebrospinal levels of tau have been found to be predictive of reductions in hippocampal volume and interpreted as reflecting neuronal loss [103]. In AD, significant amounts of Fe are found within Aβ plaques and tau-based neurofibrillary proteins [104–106]. Although Fe promotes Aβ aggregation, and binds to the Aβ peptide with binding affinity increasing Aβ aggregation, further potentiating Aβ neurotoxicity [107, 108], changes in Aβ were not found in these studies. It is possible that Aβ pathology needs to be evaluated in a transgenic mouse line with relevance to human AD protein production or requires more protracted exposures. Further, additional assessments of tau levels are needed given the lower levels of tau in air females, although these levels are consistent with prior reports [109].

A distinct effect found in males included a significant increase in volume of the substantia nigra pars compacta, the site of dopamine cell loss leading to motor dysfunction in male-dominated PD. The increase seen in substantia nigra volume is notable, given reports of enlarged substantia nigra hyperechogenicity that have been shown to correlate with Fe accumulation in substantia nigra [110], and constitute a predictive risk for PD [111]. Notably, reductions in striatal dopamine turnover were observed concurrently. The increase in substantia nigra pars compacta volume seen here in males, again, could reflect an early compensatory response to Fe inhalation {Blesa, 2017 112] and emphasizes the need to further understand compensatory responses particularly during the early trajectory of this disease. Additional studies are also needed to assess the relationship of hyperechogenicity to changes assessed by neuroimaging, as efforts to date have not been conclusive [113]. In addition, assessment of potential neuropathology, such as quantifying the extent of neuronal swelling—an indicator of neuronal damage, in this region could further define the meaning of the increased volume. Males likewise showed changes in fractional anisotropy values for a range of brain structures, most of which involved reductions, including nuclei of the amygdala, the hypoglossal nucleus, the pretectal region, and the trigeminal nerve, all of which are ultimately directly or indirectly interconnected via the trigeminal nerve. The reductions in FA could suggest the potential for demyelination, inflammation, edema and axonal loss. Moreover, these findings are consistent with a significant reduction in volume of the trigeminal nerve that was also observed in males.

Other studies of Fe inhalation suggest potential mechanistic bases for the deficits seen here. For example, Fe inhalation was found to increase numbers of activated microglial cells and levels of Il-1β in olfactory bulb of adult female mice after a 6 h/day, 5 days/week for 5 week exposure to 200 $\mu g/m^3$ iron-soot inhalation that included 40 $\mu g/m^3$ of Fe_2O_3 nanoparticles [78]. Inhaled Fe nanoparticles have also been reported to produce focal damage to the myelin sheath of a nerve fiber in the olfactory bulb [114], consistent with the fact that Fe is requisite for myelination [115]. Interestingly, no effects on brain connectivity were observed in either Fe exposed male or female brains in the current study. Future studies are needed to evaluate whether a more protracted exposure duration or prolonged aging would reveal effects of Fe inhalation on the neural connectome or neural cell subpopulations. Moreover, sex differences in astrocyte function, neuronal function, and neuronal numbers may underlie some of the sex differences observed in this study and should be investigated in future work.

Increased oxidative stress is another feature of neurodegenerative diseases, including AD [116] and PD [117], reflecting impairments in antioxidant capacity [118, 119]. Evidence for such alterations was seen in both sexes in the current study. In the case of females, this included increases in striatal glutathione even at 48 h post exposure, but not seen post-behavioral testing. Typically, reductions in glutathione have been associated with mild cognitive impairment and cognitive decline in AD [116, 120] that are considered to promote Aβ deposition and tau phosphorylation [121] and lead to apoptosis [122]. In the current study, the increase measured in females shortly after the end of the exposure period could represent an adaptive or compensatory response. Correspondingly, in a study of Fe exposure in SH-SY5Y cells, a biphasic GSH response occurred with increases followed by decreases, as Fe exposure concentration increased [123]. Of further note, however, were the concurrent increases in female striatal levels of glutamate and its precursor, glutamine, both of which are involved in ferroptotic processes, a form of cell death arising from Fe accumulation and consequent oxidative stress and lipid peroxidation. Specifically, glutamate inhibits cystine uptake by the cystine/glutamate antiporter requisite to

the production of glutathione [124]. In the case of males, glutathione increases were also seen, but not until post-behavioral testing. In conjunction with the differences in outcomes of Fe inhalation by sex, the differences in timing of the increases in glutathione suggest the potential for sex differences in antioxidant response/timing that likely contributes to the sex differences in neurodegenerative disease prevalence/phenotypes. Such differences are consistent with known sex differences in redox homeostasis in brain [125]. Differences in circulating steroid hormone levels could also contribute these sex differences and thus, should be investigated in future studies [126]. Clearly, additional markers of Fe-induced oxidative stress and ferroptosis will be required to determine the extant mechanisms underlying these changes and their inter-relationships.

The sex-related differences in response to Fe seen in this study are consistent with a significant literature documenting sex differences in Fe handling and response [1, 62, 127, 128]. Of particular relevance to the issue of critical periods of exposure, our prior studies have shown that male brain appeared to be more sensitive to inhaled Fe than female brain when such exposures were carried out developmentally in conjunction with exposures to SO_2, another component of AP, which has been shown to enhance the uptake of Fe into the central nervous system [129]. Under those conditions, effects of inhalational exposures of C57Bl/6 J mice to much lower levels of Fe nanoparticles (1 $\mu g/m^3$) in conjunction with SO_2 (500 ppb from postnatal days 4–7 and 10–13 (human third trimester brain equivalent; [130]) for 4 h/day, were particularly dramatic in males, and included a marked brain metal dyshomeostasis in frontal cortex along with striatal excitatory:inhibitory (glutamate) imbalance and marked increases in levels of dopamine and metabolites, concurrently with reductions in serotonin and metabolites at postnatal day 14 [131]. Consequently, in addition to sex, timing of exposure and potential cumulative exposures, the chemical speciation of the Fe in air pollution is an additional modifier of neurotoxicity.

As previously noted, AP that includes Fe as a contaminant represents a lifelong exposure. Whether early exposures result in developmental reprogramming of brain systems with long term consequences or whether and how the profile of effects observed in the current study would change with more protracted or more cumulative Fe inhalation exposures are all as yet unknown. Findings from the current study underscore the need for defining vulnerable periods of exposure, and assessment of both cumulative exposures and of the longitudinal trajectory of Fe-related brain impacts, as well as the mechanisms that contribute to sex and brain region differences in vulnerability to inhaled Fe.

Conclusions

The current study demonstrates that inhaled exogenous Fe UFPs indeed reach brain, where, in female brain it can produce features characteristic of AD, while in male brain it can alter volume of regions involved in PD. Levels of UFPs, considered the most reactive component of AP, are not regulated by the United States Environmental Protection Agency given monitoring complications and based, in part, on the assumption that UFP concentrations would decline with regulated reductions in levels of $PM_{2.5}$. However, this assumption has not necessarily proven to be the case, which in fact, can be inversely related [132–134]. Findings from the current study underscore the need to further understand the potential neurotoxic consequences of metal constituents within UFPs, especially Fe as it is an essential, redox active metal that has already known to be elevated in brain in numerous neurodegenerative diseases. Further studies of inhaled Fe could yield information ultimately critical to understanding mechanisms of neurodegeneration. Additionally, evidence from the current studies suggests that regulation of Fe levels in AP, and, in particular, in areas of high concentrations such as subways, might provide public health protection against a broad set of neurodegenerative diseases and disorders.

Supplementary Information

The online version contains supplementary material available at https://doi.org/10.1186/s12989-025-00622-z.

Additional file 1: Group mean ± standard error levels of locomotor activity plotted in 5 min bins across a 60 min session for males (blue) and females (red) exposed to filtered air (closed symbols) or inhaled Fe (open symbols) including ambulatory distance (top left), ambulatory time (top right), jump time (middle left), stereotypic time (middle right), resting time (bottom left) and vertical time (bottom right).

Acknowledgements
We would like to thank the University of Rochester Electron Microscopy Shared Resource Laboratory for their assistance in processing tissue for Electron Microscopy and Spectroscopy techniques.

Author contributions
DAC-S, MS and GO designed the study and prepared the manuscript; DC and RG carried out and monitored all exposures; JVG, AM, KW KC and EM carried out measurements of outcome variables; UG carried out Fe speciation analyses in TEM grids and olfactory bulb; J.A.G. and K.X carried out the magnetic resonance histology and diffusivity analyses. All authors read and approved the final manuscript.

Funding
Supported by NIH grants R01 ES032260 (Cory-Slechta, PI), R35 ES031689-01A1 (Cory-Slechta, PI), RF1 NS139187 (Sobolewski Terry, PI) and P30 ES001247 (Lawrence, PI).

Availability of data and materials
No datasets were generated or analysed during the current study.

Declarations

Ethics approval and consent to participation

This study was carried out in accordance with relevant guidelines and regulations. All mice used were treated according to protocols approved by the University of Rochester Medical Center Institutional Animal Care and Use Committee and Committee on Animal Resources (approval #102208/2010-046E) and in accordance with NIH guidelines.

Consent for publication

Not applicable.

Competing interests

The authors declare that they have no competing interests.

Author details

[1]Department of Environmental Medicine, University of Rochester Medical Center, Rochester, NY 14642, USA. [2]Mass Spectrometry Core, University of Rochester Medical Center, Rochester, NY 14642, USA. [3]Faraday Energy, Coldstream Research Park, Lexington, KY 40511, USA. [4]Department of Radiology, Duke University School of Medicine, Durham, NC 27710, USA.

Received: 22 October 2024 Accepted: 23 February 2025
Published online: 01 May 2025

References

1. Baringer SL, Simpson IA, Connor JR. Brain iron acquisition: an overview of homeostatic regulation and disease dysregulation. J Neurochem. 2023. https://doi.org/10.1111/jnc.15819.
2. Benarroch EE. Brain iron homeostasis and neurodegenerative disease. Neurology. 2009;72(16):1436. https://doi.org/10.1212/WNL.0b013e3181a26b30.
3. Dusek P, Hofer T, Alexander J, Roos PM, Aaseth JO. Cerebral iron deposition in neurodegeneration. Biomolecules. 2022;12:5. https://doi.org/10.3390/biom12050714.
4. Tao Y, Wang Y, Rogers JT, Wang F. Perturbed iron distribution in Alzheimer's disease serum, cerebrospinal fluid, and selected brain regions: a systematic review and meta-analysis. J Alzheimers Dis. 2014;42(2):679–90. https://doi.org/10.3233/JAD-140396.
5. Connor JR, Menzies SL, St Martin SM, Mufson EJ. A histochemical study of iron, transferrin, and ferritin in Alzheimer's diseased brains. J Neurosci Res. 1992;31(1):75–83. https://doi.org/10.1002/jnr.490310111.
6. van Duijn S, Bulk M, van Duinen SG, Nabuurs RJA, van Buchem MA, van der Weerd L, et al. Cortical iron reflects severity of Alzheimer's disease. J Alzheimers Dis. 2017;60(4):1533–45. https://doi.org/10.3233/JAD-161143.
7. Li KR, Avecillas-Chasin J, Nguyen TD, Gillen KM, Dimov A, Chang E, et al. Quantitative evaluation of brain iron accumulation in different stages of Parkinson's disease. J Neuroimaging. 2022;32(2):363–71. https://doi.org/10.1111/jon.12957.
8. Mochizuki H, Choong CJ, Baba K. Parkinson's disease and iron. J Neural Transm (Vienna). 2020;127(2):181–7. https://doi.org/10.1007/s00702-020-02149-3.
9. Penke L, Valdés Hernandéz MC, Maniega SM, Gow AJ, Murray C, Starr JM, et al. Brain iron deposits are associated with general cognitive ability and cognitive aging. Neurobiol Aging. 2012;33(3):510-7.e2. https://doi.org/10.1016/j.neurobiolaging.2010.04.032.
10. Ding B, Chen K-M, Ling H-W, Sun F, Li X, Wan T, et al. Correlation of iron in the hippocampus with MMSE in patients with Alzheimer's disease. J Magn Reson Imaging: JMRI. 2009;29(4):793–8. https://doi.org/10.1002/jmri.21730.10.1002/jmri.21730.
11. Smith MA, Zhu X, Tabaton M, Liu G, McKeel DW Jr, Cohen ML, et al. Increased iron and free radical generation in preclinical Alzheimer disease and mild cognitive impairment. J Alzheimers Dis. 2010;19(1):363–72. https://doi.org/10.3233/jad-2010-1239.
12. Baiano C, Barone P, Trojano L, Santangelo G. Prevalence and clinical aspects of mild cognitive impairment in Parkinson's disease: a meta-analysis. Mov Disord. 2020;35(1):45–54. https://doi.org/10.1002/mds.27902.
13. Li Y, Jiao Q, Xu H, Du X, Shi L, Jia F, et al. Biometal dyshomeostasis and toxic metal accumulations in the development of Alzheimer's disease. Front Mol Neurosci. 2017;10:339. https://doi.org/10.3389/fnmol.2017.00339.
14. Chen X, Pang X, Yeo AJ, Xie S, Xiang M, Shi B, et al. The molecular mechanisms of ferroptosis and its role in blood-brain barrier dysfunction. Front Cell Neurosci. 2022;16:889765. https://doi.org/10.3389/fncel.2022.889765.
15. Reff A, Bhave PV, Simon H, Pace TG, Pouliot GA, Mobley JD, et al. Emissions inventory of PM2.5 trace elements across the United States. Environ Sci Technol. 2009;15:5790–6. https://doi.org/10.1021/es802930x.10.1021/es802930x.
16. Kwon H-S, Ryu MH, Carlsten C. Ultrafine particles: unique physicochemical properties relevant to health and disease. Exp Mol Med. 2020;52(3):318–28. https://doi.org/10.1038/s12276-020-0405-1.10.1038/s12276-020-0405-1.
17. Lin CC, Chen SJ, Huang KL, Hwang WI, Chang-Chien GP, Lin WY. Characteristics of metals in nano/ultrafine/fine/coarse particles collected beside a heavily trafficked road. Environ Sci Technol. 2005;39(21):8113–22.
18. Oberdorster G, Sharp Z, Atudorei V, Elder A, Gelein R, Kreyling W, et al. Translocation of inhaled ultrafine particles to the brain. Inhal Toxicol. 2004;6–7:437–45.
19. Graham UM, Dozier AK, Oberdorster G, Yokel RA, Molina R, Brain JD, et al. Tissue specific fate of nanomaterials by advanced analytical imaging techniques—a review. Chem Res Toxicol. 2020;5:1145–62. https://doi.org/10.1021/acs.chemrestox.0c00072.
20. Gellein K, Syversen T, Steinnes E, Nilsen TI, Dahl OP, Mitrovic S, et al. Trace elements in serum from patients with Parkinson's disease–a prospective case-control study: the Nord-Trøndelag Health Study (HUNT). Brain Res. 2008;1219:111–5. https://doi.org/10.1016/j.brainres.2008.05.002.
21. Alimonti A, Ristori G, Giubilei F, Stazi MA, Pino A, Visconti A, et al. Serum chemical elements and oxidative status in Alzheimer's disease, Parkinson disease and multiple sclerosis. Neurotoxicology. 2007;28(3):450–6. https://doi.org/10.1016/j.neuro.2006.12.001.
22. Gong Y, Zhang X, Zhao X, Chang H, Zhang J, Gao Z, et al. Global ambient particulate matter pollution and neurodegenerative disorders: a systematic review of literature and meta-analysis. Environ Sci Pollut Res Int. 2023;30(14):39418–30. https://doi.org/10.1007/s11356-023-25731-0.
23. Cory-Slechta DA, Sobolewski M. Neurotoxic effects of air pollution: an urgent public health concern. Nat Rev Neurosci. 2023;24(3):129–30. https://doi.org/10.1038/s41583-022-00672-8.
24. Fu P, Yung KKL. Air pollution and Alzheimer's disease: a systematic review and meta-analysis. J Alzheimers Dis. 2020;77(2):701–14. https://doi.org/10.3233/JAD-200483.
25. Cheng S, Jin Y, Dou Y, Zhao Y, Duan Y, Pei H, et al. Long-term particulate matter 2.5 exposure and dementia: a systematic review and meta-analysis. Public Health. 2022;212:33–41. https://doi.org/10.1016/j.puhe.2022.08.006.
26. Hu CY, Fang Y, Li FL, Dong B, Hua XG, Jiang W, et al. Association between ambient air pollution and Parkinson's disease: systematic review and meta-analysis. Environ Res. 2019;168:448–59. https://doi.org/10.1016/j.envres.2018.10.008.
27. Weuve J, Puett RC, Schwartz J, Yanosky JD, Laden F, Grodstein F. Exposure to particulate air pollution and cognitive decline in older women. Arch Intern Med. 2012;172(3):219–27. https://doi.org/10.1001/archinternmed.2011.683.
28. Cacciottolo M, Wang X, Driscoll I, Woodward N, Saffari A, Reyes J, et al. Particulate air pollutants, APOE alleles and their contributions to cognitive impairment in older women and to amyloidogenesis in experimental models. Transl Psychiatry. 2017;7(1):e1022. https://doi.org/10.1038/tp.2016.280.
29. Mo S, Wang Y, Peng M, Wang Q, Zheng H, Zhan Y, et al. Sex disparity in cognitive aging related to later-life exposure to ambient air pollution. Sci Total Environ. 2023;886:163980. https://doi.org/10.1016/j.scitotenv.2023.163980.
30. Jo S, Kim YJ, Park KW, Hwang YS, Lee SH, Kim BJ, et al. Association of NO2 and other air pollution exposures with the risk of parkinson

disease. JAMA Neurol. 2021;78(7):800–8. https://doi.org/10.1001/jamaneurol.2021.1335.
31. Paul KC, Haan M, Mayeda ER, Ritz BR. Ambient air pollution, noise, and late-life cognitive decline and dementia risk. Annu Rev Public Health. 2019;40:203–20. https://doi.org/10.1146/annurev-publhealth-040218-044058.
32. Kilian J, Kitazawa M. The emerging risk of exposure to air pollution on cognitive decline and Alzheimer's disease—evidence from epidemiological and animal studies. Biomed J. 2018;41(3):141–62. https://doi.org/10.1016/j.bj.2018.06.001.
33. Hedges DW, Erickson LD, Kunzelman J, Brown BL, Gale SD. Association between exposure to air pollution and hippocampal volume in adults in the UK Biobank. Neurotoxicology. 2019;74:108–20. https://doi.org/10.1016/j.neuro.2019.06.005.
34. Wu J, Ning Y, Gao Y, Shan R, Wang B, Lv J, et al. Association between ambient air pollution and MRI-defined brain infarcts in health examinations in China. Int J Environ Res Public Health. 2021;18:8. https://doi.org/10.3390/ijerph18084325.
35. Wilker EH, Preis SR, Beiser AS, Wolf PA, Au R, Kloog I, et al. Long-term exposure to fine particulate matter, residential proximity to major roads and measures of brain structure. Stroke. 2015;46(5):1161–6.
36. Casanova R, Wang X, Reyes J, Akita Y, Serre ML, Vizuete W, et al. A voxel-based morphometry study reveals local brain structural alterations associated with ambient fine particles in older women. Front Hum Neurosci. 2016;10:495.
37. Chen JC, Wang X, Wellenius GA, Serre ML, Driscoll I, Casanova R, et al. Ambient air pollution and neurotoxicity on brain structure: evidence from Women's Health Initiative Memory Study. Ann Neurol. 2015. https://doi.org/10.1002/ana.24460.
38. Power MC, Adar SD, Yanosky JD, Weuve J. Exposure to air pollution as a potential contributor to cognitive function, cognitive decline, brain imaging, and dementia: a systematic review of epidemiologic research. Neurotoxicology. 2016;1:2–3.
39. Patten KT, Valenzuela AE, Wallis C, Berg EL, Silverman JL, Bein KJ, et al. The effects of chronic exposure to ambient traffic-related air pollution on Alzheimer's disease phenotypes in wildtype and genetically predisposed male and female rats. Environ Health Perspect. 2021;129(5):57005. https://doi.org/10.1289/ehp8905.
40. Chen TC, Lo YC, Li SJ, Lin YC, Chang CW, Liang YW, et al. Assessing traffic-related air pollution-induced fiber-specific white matter degradation associated with motor performance declines in aged rats. Ecotoxicol Environ Saf. 2023;263:115373. https://doi.org/10.1016/j.ecoenv.2023.115373.
41. Chen JC, Schwartz J. Neurobehavioral effects of ambient air pollution on cognitive performance in US adults. Neurotoxicology. 2009;30(2):231–9. https://doi.org/10.1016/j.neuro.2008.12.011.
42. Chen LC, Lippmann M. Effects of metals within ambient air particulate matter (PM) on human health. Inhal Toxicol. 2009;21(1):1–31. https://doi.org/10.1080/08958370802105405.
43. Loxham M, Nieuwenhuijsen MJ. Health effects of particulate matter air pollution in underground railway systems—a critical review of the evidence. Part Fibre Toxicol. 2019;16(1):1–24.
44. Chillrud SN, Grass D, Ross JM, Coulibaly D, Slavkovich V, Epstein D, et al. Steel dust in the New York City subway system as a source of manganese, chromium, and iron exposures for transit workers. J Urban Health. 2005;82(1):33–42.
45. Luglio DG, Katsigeorgis M, Hess J, Kim R, Adragna J, Raja A, et al. PM 25 concentration and composition in subway systems in the Northeastern United States. Environ Health Perspect. 2021;129(2):027001.
46. Cartledge BT, Majestic BJ. Metal concentrations and soluble iron speciation in fine particulate matter from light rail activity in the Denver-Metropolitan area. Atmos Pollut Res. 2015;6(3):495–502. https://doi.org/10.5094/APR.2015.
47. Moreno T, Martins V, Querol X, Jones T, BéruBé K, Minguillón MC, et al. A new look at inhalable metalliferous airborne particles on rail subway platforms. Sci The Total Environ. 2015;505:367–75. https://doi.org/10.1016/j.scitotenv.2014.10.013.
48. Chen Y, Shah N, Huggins FE, Huffman GP. Microanalysis of ambient particles from Lexington, KY, by electron microscopy. Atmos Environ. 2006;40(4):651–63. https://doi.org/10.1016/j.atmosenv.2005.09.036.
49. Russell EWB, Rampino MR, Puffer JH. Distribution and origin of magnetite spherules in air, waters, and sediments of the greater New York City area and the North Atlantic ocean. J Sediment Res. 1980;50(1):247–56. https://doi.org/10.1306/212F79BE-2B24-11D7-8648000102C1865D.
50. Kukutschová J, Moravec P, Tomášek V, Matějka V, Smolík J, Schwarz J, et al. On airborne nano/micro-sized wear particles released from low-metallic automotive brakes. Environ Pollut. 2011;159(4):998–1006. https://doi.org/10.1016/j.envpol.2010.11.036.
51. Maher BA. Airborne magnetite- and iron-rich pollution nanoparticles: potential neurotoxicants and environmental risk factors for neurodegenerative disease. Including Alzheimer's Dis. 2019;71(2):361–75. https://doi.org/10.3233/JAD-190204.
52. Hautot D, Pankhurst QA, Khan N, Dobson J. Preliminary evaluation of nanoscale biogenic magnetite in Alzheimer's disease brain tissue. Proc Biol Sci. 2003;270(Suppl 1):S62–4. https://doi.org/10.1098/rsbl.2003.0012.
53. Pankhurst Q, Hautot D, Khan N, Dobson J. Increased levels of magnetic iron compounds in Alzheimer's disease. J Alzheimers Dis. 2008;13(1):49–52.
54. Plascencia-Villa G, Ponce A, Collingwood JF, Arellano-Jimenez MJ, Zhu X, Rogers JT, et al. High-resolution analytical imaging and electron holography of magnetite particles in amyloid cores of Alzheimer's disease. Sci Rep. 2016;6:24873–81. https://doi.org/10.1038/srep24873.
55. Telling ND, Everett J, Collingwood JF, Dobson J, van der Laan G, Gallagher JJ, et al. Iron Biochemistry is Correlated with Amyloid Plaque Morphology in an Established Mouse Model of Alzheimer's Disease. Cell Chem Biol. 2017;24 10:1205–15 e3; https://doi.org/10.1016/j.chembiol.2017.07.014.
56. Cory-Slechta DA, Merrill A, Sobolewski M. Air pollution-related neurotoxicity across the life span. Annu Rev Pharmacol Toxicol. 2023;63:143–63. https://doi.org/10.1146/annurev-pharmtox-051921-020812.
57. OECD. Test No. 412: Subacute Inhalation Toxicity: 28-Day Study. 2018.
58. Johnson GA, Tian Y, Ashbrook DG, Cofer GP, Cook JJ, Gee JC, et al. Merged magnetic resonance and light sheet microscopy of the whole mouse brain. Proc Natl Acad Sci USA. 2023;120(17):e2218617120.
59. Wang N, Anderson RJ, Badea A, Cofer G, Dibb R, Qi Y, et al. Whole mouse brain structural connectomics using magnetic resonance histology. Brain Struct Funct. 2018;223(9):4323–35. https://doi.org/10.1007/s00429-018-1750-x.
60. Wang N, White LE, Qi Y, Cofer G, Johnson GA. Cytoarchitecture of the mouse brain by high resolution diffusion magnetic resonance imaging. Neuroimage. 2020;216:116876. https://doi.org/10.1016/j.neuroimage.2020.116876.
61. Wong JM, Malec PA, Mabrouk OS, Ro J, Dus M, Kennedy RT. Benzoyl chloride derivatization with liquid chromatography-mass spectrometry for targeted metabolomics of neurochemicals in biological samples. J Chromatogr A. 2016;1446:78–90. https://doi.org/10.1016/j.chroma.2016.04.006.
62. Wade QW, Chiou B, Connor JR. Iron uptake at the blood-brain barrier is influenced by sex and genotype. Adv Pharmacol. 2019;84:123–45. https://doi.org/10.1016/bs.apha.2019.02.005.
63. Pan W, Chen H, Ni C, Zong G, Yuan C, Yang M. Sex-specific associations of dietary iron intake with brain iron deposition on imaging and incident dementia: a prospective cohort study. J Nutr Health Aging. 2022;26(10):954–61. https://doi.org/10.1007/s12603-022-1852-2.
64. Thulluri S, Wu M, Blough ER, Manne ND, Litchfield AB, Wang B. Regulation of iron-related molecules in the rat hippocampus: sex- and age-associated differences. Ann Clin Lab Sci. 2012;42(2):145–51.
65. DuMont M, Agostinis A, Singh K, Swan E, Buttle Y, Tropea D. Sex representation in neurodegenerative and psychiatric disorders' preclinical and clinical studies. Neurobiol Dis. 2023;184:106214.
66. Winham SJ, Mielke MM. What about sex? Nat Metab. 2021;3(12):1586–8. https://doi.org/10.1038/s42255-021-00503-7.
67. Cohen J. Statistical power analysis for the behavioral sciences. 2nd ed. Hillsdale, NJ: Lawrence Erlbaum Associates Publishers; 1988.
68. Faul F, Erdfelder E, Lang A-G, Buchner A. G*Power 3: A flexible statistical power analysis program for the social, behavioral, and biomedical sciences. Behav Res Methods. 2007;39:175–91.
69. Tjalve H, Henriksson J. Uptake of metals in the brain via olfactory pathways. Neurotoxicology. 1999;20(2–3):181–95.

70. Wang B, Feng WY, Wang M, Shi JW, Zhang F, Ouyang H, et al. Transport of intranasally instilled fine Fe2O3 particles into the brain: micro-distribution, chemical states, and histopathological observation. Biol Trace Elem Res. 2007;118(3):233–43.
71. Petters C, Bulcke F, Thiel K, Bickmeyer U, Dringen R. Uptake of fluorescent iron oxide nanoparticles by oligodendroglial OLN-93 cells. Neurochem Res. 2014;39(2):372–83. https://doi.org/10.1007/s11064-013-1234-6.
72. Persson E, Henriksson J, Tjalve H. Uptake of cobalt from the nasal mucosa into the brain via olfactory pathways in rats. Toxicol Lett. 2003;145(1):19–27.
73. Sunderman FW Jr. Nasal toxicity, carcinogenicity, and olfactory uptake of metals. Ann Clin Lab Sci. 2001;31(1):3–24.
74. Perl D, Good P. Uptake of aluminium into central nervous system along nasal-olfactory pathways. The Lancet. 1987;329(8540):1028. https://doi.org/10.1016/S0140-6736(87)92288-4.
75. Hunter DD, Dey RD. Identification and neuropeptide content of trigeminal neurons innervating the rat nasal epithelium. Neuroscience. 1998;83(2):591–9.
76. Maher BA, Ahmed IA, Karloukovski V, MacLaren DA, Foulds PG, Allsop D, et al. Magnetite pollution nanoparticles in the human brain. Proc Natl Acad Sci USA. 2016;113(39):10797–801. https://doi.org/10.1073/pnas.1605941113.
77. Vanbrabant K, Van Dam D, Bongaerts E, Vermeiren Y, Bové H, Hellings N, et al. Accumulation of ambient black carbon particles within key memory-related brain regions. JAMA Netw Open. 2024;7(4):e245678. https://doi.org/10.1001/jamanetworkopen.2024.5678.
78. Hopkins LE, Laing EA, Peake JL, Uyeminami D, Mack SM, Li X, et al. Repeated iron-soot exposure and nose-to-brain transport of inhaled ultrafine particles. Toxicol Pathol. 2018;46(1):75–84. https://doi.org/10.1177/0192623317729222.
79. Hawkes CH, Del Tredici K, Braak H. Parkinson's disease: a dual-hit hypothesis. Neuropathol Appl Neurobiol. 2007;33(6):599–614.
80. Jobin B, Boller B, Frasnelli J. Volumetry of olfactory structures in mild cognitive impairment and alzheimer's disease: a systematic review and a meta-analysis. Brain Sci. 2021;11(8):1010. https://doi.org/10.3390/brainsci11081010.
81. Barber AJ, Del Genio CL, Swain AB, Pizzi EM, Watson SC, Tapiavala VN, et al. Age, sex and Alzheimer's disease: a longitudinal study of 3xTg-AD mice reveals sex-specific disease trajectories and inflammatory responses mirrored in postmortem brains from Alzheimer's patients. Alzheimers Res Ther. 2024;16(1):134. https://doi.org/10.1186/s13195-024-01492-x.
82. Winklewski PJ, Sabisz A, Naumczyk P, Jodzio K, Szurowska E, Szarmach A. Understanding the physiopathology behind axial and radial diffusivity changes-what do we know? Front Neurol. 2018;9:92. https://doi.org/10.3389/fneur.2018.00092.
83. Klocke C, Allen JL, Sobolewski M, Blum JL, Zelikoff JT, Cory-Slechta DA. Exposure to fine and ultrafine particulate matter during gestation alters postnatal oligodendrocyte maturation, proliferation capacity, and myelination. Neurotoxicology. 2017. https://doi.org/10.1016/j.neuro.2017.10.004.
84. Klocke C, Allen JL, Sobolewski M, Mayer-Proschel M, Blum JL, Lauterstein D, et al. Neuropathological consequences of gestational exposure to concentrated ambient fine and ultrafine particles in the mouse. Toxicol Sci. 2017;156(2):492–508. https://doi.org/10.1093/toxsci/kfx010.
85. Allen JL, Oberdorster G, Morris-Schaffer K, Wong C, Klocke C, Sobolewski M, et al. Developmental neurotoxicity of inhaled ambient ultrafine particle air pollution: Parallels with neuropathological and behavioral features of autism and other neurodevelopmental disorders. Neurotoxicology. 2017;59:140–54. https://doi.org/10.1016/j.neuro.2015.12.014.
86. Borghammer P, Just MK, Horsager J, Skjærbæk C, Raunio A, Kok EH, et al. A postmortem study suggests a revision of the dual-hit hypothesis of Parkinson's disease. NPJ Parkinsons Dis. 2022;8(1):166. https://doi.org/10.1038/s41531-022-00436-2.
87. Gardner B, Dieriks BV, Cameron S, Mendis LHS, Turner C, Faull RLM, et al. Metal concentrations and distributions in the human olfactory bulb in Parkinson's disease. Sci Rep. 2017;7(1):10454. https://doi.org/10.1038/s41598-017-10659-6.
88. Murray HC, Dieriks BV, Swanson MEV, Anekal PV, Turner C, Faull RLM, et al. The unfolded protein response is activated in the olfactory system in Alzheimer's disease. Acta Neuropathol Commun. 2020;8(1):109. https://doi.org/10.1186/s40478-020-00986-7.
89. Kovács T, Cairns NJ, Lantos PL. Olfactory centres in Alzheimer's disease: olfactory bulb is involved in early Braak's stages. NeuroReport. 2001;12(2):285–8. https://doi.org/10.1097/00001756-200102120-00021.
90. Takeda A, Baba T, Kikuchi A, Hasegawa T, Sugeno N, Konno M, et al. Olfactory dysfunction and dementia in Parkinson's disease. J Parkinsons Dis. 2014;4(2):181–7. https://doi.org/10.3233/jpd-130277.
91. Aqrabawi AJ, Kim JC. Hippocampal projections to the anterior olfactory nucleus differentially convey spatiotemporal information during episodic odour memory. Nat Commun. 2018;9(1):2735. https://doi.org/10.1038/s41467-018-05131-6.
92. Vereecken TH, Vogels OJ, Nieuwenhuys R. Neuron loss and shrinkage in the amygdala in Alzheimer's disease. Neurobiol Aging. 1994;15(1):45–54. https://doi.org/10.1016/0197-4580(94)90143-0.
93. Wang Z, Zhang M, Han Y, Song H, Guo R, Li K. Differentially disrupted functional connectivity of the subregions of the amygdala in Alzheimer's disease. J Xray Sci Technol. 2016;24(2):329–42. https://doi.org/10.3233/xst-160556.
94. Ferreyra-Moyano H, Barragan E. The olfactory system and Alzheimer's disease. Int J Neurosci. 1989;49(3–4):157–97. https://doi.org/10.3109/00207458909084824.
95. Baloyannis SJ, Manolidis SL, Manolidis LS. Synaptic alterations in the vestibulocerebellar system in Alzheimer's disease—a Golgi and electron microscope study. Acta Otolaryngol. 2000;120(2):247–50. https://doi.org/10.1080/000164800750001026.
96. Mavroudis I. Cerebellar pathology in Alzheimer's disease. Hell J Nucl Med. 2019;22(Suppl):174–9.
97. Koudinov A, Kezlya E, Koudinova N, Berezov T. Amyloid-beta, tau protein, and oxidative changes as a physiological compensatory mechanism to maintain CNS plasticity under Alzheimer's disease and other neurodegenerative conditions. J Alzheimers Dis. 2009;18(2):381–400. https://doi.org/10.3233/jad-2009-1202.
98. Rao SS, Adlard PA. Untangling tau and iron: exploring the interaction between iron and tau in neurodegeneration. Front Mol Neurosci. 2018;11:276. https://doi.org/10.3389/fnmol.2018.00276.
99. Yamamoto A, Shin RW, Hasegawa K, Naiki H, Sato H, Yoshimasu F, et al. Iron (III) induces aggregation of hyperphosphorylated tau and its reduction to iron (II) reverses the aggregation: implications in the formation of neurofibrillary tangles of Alzheimer's disease. J Neurochem. 2002;82(5):1137–47. https://doi.org/10.1046/j.1471-4159.2002.t01-1-01061.x.
100. Aschenbrenner AJ, Gordon BA, Benzinger TLS, Morris JC, Hassenstab JJ. Influence of tau PET, amyloid PET, and hippocampal volume on cognition in Alzheimer disease. Neurology. 2018;91(9):e859–66. https://doi.org/10.1212/wnl.0000000000006075.
101. Devous MD Sr, Fleisher AS, Pontecorvo MJ, Lu M, Siderowf A, Navitsky M, et al. Relationships between cognition and neuropathological Tau in Alzheimer's disease assessed by 18F Flortaucipir PET. J Alzheimers Dis. 2021;80(3):1091–104. https://doi.org/10.3233/jad-200808.
102. Richter N, Bischof GN, Dronse J, Nellessen N, Neumaier B, Langen KJ, et al. Entorhinal tau predicts hippocampal activation and memory deficits in Alzheimer's disease. J Alzheimers Dis. 2020;78(4):1601–14. https://doi.org/10.3233/jad-200835.
103. de Souza LC, Chupin M, Lamari F, Jardel C, Leclercq D, Colliot O, et al. CSF tau markers are correlated with hippocampal volume in Alzheimer's disease. Neurobiol Aging. 2012;33(7):1253–7. https://doi.org/10.1016/j.neurobiolaging.2011.02.022.
104. Smith MA, Harris PL, Sayre LM, Perry G. Iron accumulation in Alzheimer disease is a source of redox-generated free radicals. Proc Natl Acad Sci USA. 1997;94(18):9866–8. https://doi.org/10.1073/pnas.94.18.9866.
105. Good PF, Olanow CW, Perl DP. Neuromelanin-containing neurons of the substantia nigra accumulate iron and aluminum in Parkinson's disease: a LAMMA study. Brain Res. 1992;593(2):343–6.
106. Huat TJ, Camats-Perna J, Newcombe EA, Valmas N, Kitazawa M, Medeiros R. Metal toxicity links to Alzheimer's disease and neuroinflammation. J Mol Biol. 2019;431(9):1843–68. https://doi.org/10.1016/j.jmb.2019.01.018.

107. Boopathi S, Kolandaivel P. Fe(2+) binding on amyloid beta-peptide promotes aggregation. Proteins. 2016;84(9):1257–74. https://doi.org/10.1002/prot.25075.
108. Becerril-Ortega J, Bordji K, Freret T, Rush T, Buisson A. Iron overload accelerates neuronal amyloid-beta production and cognitive impairment in transgenic mice model of Alzheimer's disease. Neurobiol Aging. 2014;35(10):2288–301. https://doi.org/10.1016/j.neurobiolaging.2014.04.019.
109. Hunter CL, Bimonte-Nelson HA, Nelson M, Eckman CB, Granholm AC. Behavioral and neurobiological markers of Alzheimer's disease in Ts65Dn mice: effects of estrogen. Neurobiol Aging. 2004;25(7):873–84. https://doi.org/10.1016/j.neurobiolaging.2003.10.010.
110. Ahmadi SA, Bötzel K, Levin J, Maiostre J, Klein T, Wein W, et al. Analyzing the co-localization of substantia Nigra hyper-echogenicities and iron accumulation in Parkinson's disease: a multi-modal atlas study with transcranial ultrasound and MRI. NeuroImage Clin. 2020;26:102185. https://doi.org/10.1016/j.nicl.2020.102185.
111. Berg D, Seppi K, Behnke S, Liepelt I, Schweitzer K, Stockner H, et al. Enlarged substantia nigra hyperechogenicity and risk for Parkinson disease: A 37-Month 3-center study of 1847 older persons. Arch Neurol. 2011;68(7):932–7. https://doi.org/10.1001/archneurol.2011.141.
112. Blesa J, Trigo-Damas I, Dileone M, Del Rey NL, Hernandez LF, Obeso JA. Compensatory mechanisms in Parkinson's disease: Circuits adaptations and role in disease modification. Exper Neurol 2017;298(Pt B):148-161. https://doi.org/10.1016/j.expneurol.2017.10.002.
113. Prasuhn J, Strautz R, Lemmer F, Dreischmeier S, Kasten M, Hanssen H, et al. Neuroimaging correlates of substantia Nigra hyperechogenicity in Parkinson's disease. J Parkinsons Dis. 2022;12(4):1191–200. https://doi.org/10.3233/jpd-213000.
114. Sutunkova MP, Katsnelson BA, Privalova LI, Gurvich VB, Konysheva LK, Shur VY, et al. On the contribution of the phagocytosis and the solubilization to the iron oxide nanoparticles retention in and elimination from lungs under long-term inhalation exposure. Toxicology. 2016;363–364:19–28. https://doi.org/10.1016/j.tox.2016.07.006.
115. Todorich B, Pasquini JM, Garcia CI, Paez PM, Connor JR. Oligodendrocytes and myelination: the role of iron. Glia. 2009;57(5):467–78. https://doi.org/10.1002/glia.20784.
116. von Bernhardi R, Eugenin J. Alzheimer's disease: redox dysregulation as a common denominator for diverse pathogenic mechanisms. Antioxid Redox Signal. 2012;16(9):974–1031. https://doi.org/10.1089/ars.2011.4082.
117. Hemmati-Dinarvand M, Saedi S, Valilo M, Kalantary-Charvadeh A, Alizadeh Sani M, Kargar R, et al. Oxidative stress and Parkinson's disease: conflict of oxidant-antioxidant systems. Neurosci Lett. 2019;709:134296. https://doi.org/10.1016/j.neulet.2019.134296.
118. Umeno A, Biju V, Yoshida Y. In vivo ROS production and use of oxidative stress-derived biomarkers to detect the onset of diseases such as Alzheimer's disease, Parkinson's disease, and diabetes. Free Radic Res. 2017;51(4):413–27. https://doi.org/10.1080/10715762.2017.1315114.
119. Cristovao JS, Santos R, Gomes CM. Metals and neuronal metal binding proteins implicated in Alzheimer's disease. Oxid Med Cell Longev. 2016. https://doi.org/10.1155/2016/9812178.
120. Yin F, Sancheti H, Patil I, Cadenas E. Energy metabolism and inflammation in brain aging and Alzheimer's disease. Free Radic Biol Med. 2016;100:108–22. https://doi.org/10.1016/j.freeradbiomed.2016.04.200.
121. Chen JH, Singh N, Tay H, Walczyk T. Imbalance of iron influx and efflux causes brain iron accumulation over time in the healthy adult rat. Metallomics. 2014;6(8):1417–26. https://doi.org/10.1039/c4mt00054d.
122. Cai Z, Zhao B, Ratka A. Oxidative stress and beta-amyloid protein in Alzheimer's disease. Neuromolecular Med. 2011;13(4):223–50. https://doi.org/10.1007/s12017-011-8155-9.
123. Aracena P, Aguirre P, Muñoz P, Núñez MT. Iron and glutathione at the crossroad of redox metabolism in neurons. Biol Res. 2006;39(1):157–65. https://doi.org/10.4067/s0716-97602006000100017.
124. Viktorinova A. Future perspectives of oxytosis/ferroptosis research in neurodegeneration diseases. Cell Mol Neurobiol. 2023. https://doi.org/10.1007/s10571-023-01353-5.
125. Ruszkiewicz JA, Miranda-Vizuete A, Tinkov AA, Skalnaya MG, Skalny AV, Tsatsakis A, et al. Sex-specific differences in redox homeostasis in brain norm and disease. J Mol Neurosci. 2019;67(2):312–42. https://doi.org/10.1007/s12031-018-1241-9.
126. Busler JN, Slate SR, Liao H, Lyndon S, Taylor J, Lin AP, et al. Sex hormones as correlates of oxidative stress in the adult brain. Psychiatry Res Neuroimaging. 2023;334:111681. https://doi.org/10.1016/j.pscychresns.2023.111681.
127. Duck KA, Neely EB, Simpson IA, Connor JR. A role for sex and a common HFE gene variant in brain iron uptake. J Cereb Blood Flow Metab. 2018;38(3):540–8. https://doi.org/10.1177/0271678x17701949.
128. Chiou B, Neely EB, McDevitt DS, Simpson IA, Connor JR. Transferrin and H-ferritin involvement in brain iron acquisition during postnatal development: impact of sex and genotype. J Neurochem. 2020;152(3):381–96. https://doi.org/10.1111/jnc.14834.
129. Watson AY, Brain JD. The effect of SO2 on the uptake of particles by mouse bronchial epithelium. Exp Lung Res. 1980;1(1):67–87.
130. Clancy B, Finlay BL, Darlington RB, Anand KJ. Extrapolating brain development from experimental species to humans. Neurotoxicology. 2007;28(5):931–7. https://doi.org/10.1016/j.neuro.2007.01.014.
131. Sobolewski M, Conrad K, Marvin E, Eckard M, Goeke CM, Merrill AK, et al. The potential involvement of inhaled iron (Fe) in the neurotoxic effects of ultrafine particulate matter air pollution exposure on brain development in mice. Particle Fibre Toxicol. 2022;19(1):56. https://doi.org/10.1186/s12989-022-00496-5.
132. Ruuskanen J, Tuch T, Brink T, Peters A, Khlystov A, Mirme A, et al. Concentrations of ultrafine, fine and PM2.5 particles in three European cities. Atmos Environ. 2001;35:3729–38.
133. Tuch T, Brand P, Wichmann HE, Heyder J. Variation of particle number and mass concentration in various size ranges of ambient aerosols in Eastern Germany. Atmos Environ. 1997;31(24):4193–7. https://doi.org/10.1016/S1352-2310(97)00260-4.
134. Knibbs LD, de Dear RJ. Exposure to ultrafine particles and PM2.5 in four Sydney transport modes. Atmos Environ. 2010;44(26):3224–7. https://doi.org/10.1016/j.atmosenv.2010.05.026.

Publisher's Note